NAVAL POSTGRADUATE SCHOOL

MONTEREY, CALIFORNIA

THESIS

MEMS TERAHERTZ FOCAL PLANE ARRAY WITH OPTICAL READOUT

by

Hugo A. Gonzalez Jr.

June 2016

Thesis Advisor:	Gamani Karunasiri
Co-Advisor:	Fabio D. P. Alves
Second Reader:	Jae Jun Kim

THIS PAGE INTENTIONALLY LEFT BLANK

REPORT DOCUMENTATION PAGE			Form Approved OMB No. 0704–0188
Public reporting burden for this collection of information is estimated to average 1 hour per response, including the time for reviewing instruction, searching existing data sources, gathering and maintaining the data needed, and completing and reviewing the collection of information. Send comments regarding this burden estimate or any other aspect of this collection of information, including suggestions for reducing this burden, to Washington headquarters Services, Directorate for Information Operations and Reports, 1215 Jefferson Davis Highway, Suite 1204, Arlington, VA 22202-4302, and to the Office of Management and Budget, Paperwork Reduction Project (0704-0188) Washington, DC 20503.			
1. AGENCY USE ONLY ***(Leave blank)***	**2. REPORT DATE** June 2016	**3. REPORT TYPE AND DATES COVERED** Master's thesis	
4. TITLE AND SUBTITLE MEMS TERAHERTZ FOCAL PLANE ARRAY WITH OPTICAL READOUT			**5. FUNDING NUMBERS**
6. AUTHOR(S) Hugo A. Gonzalez Jr.			
7. PERFORMING ORGANIZATION NAME(S) AND ADDRESS(ES) Naval Postgraduate School Monterey, CA 93943-5000			**8. PERFORMING ORGANIZATION REPORT NUMBER**
9. SPONSORING /MONITORING AGENCY NAME(S) AND ADDRESS(ES) N/A			**10. SPONSORING / MONITORING AGENCY REPORT NUMBER**
11. SUPPLEMENTARY NOTES The views expressed in this thesis are those of the author and do not reflect the official policy or position of the Department of Defense or the U.S. Government. IRB Protocol number ____N/A____.			
12a. DISTRIBUTION / AVAILABILITY STATEMENT Approved for public release; distribution is unlimited			**12b. DISTRIBUTION CODE**

13. ABSTRACT (maximum 200 words)

The terahertz (THz) spectral range remains a relatively untapped portion of the electromagnetic spectrum. THz radiation's unique ability to penetrate non-metallic materials presents an exciting opportunity for many imaging applications. The purpose of this research is to investigate a unique imaging method using a THz radiation source and metamaterial absorber. By using a metamaterial absorber, the THz detection frequency of interest can be tuned by controlling geometrical parameters with nearly 100% absorption. THz sensing can be achieved by integrating a metamaterial absorber with bi-material legs to form a sensor. Moveable mirror-like surfaces on the backside of the metamaterial under THz absorption can cause a deflection of visible light and from it, the original image can be reconstructed using an optical readout system. In this thesis, the construction of the optical readout system for characterization of sensor pixels as well as THz imaging is described.

14. SUBJECT TERMS THz, terahertz, QCL, metamaterial, imaging, optical readout			**15. NUMBER OF PAGES** 89
			16. PRICE CODE
17. SECURITY CLASSIFICATION OF REPORT Unclassified	**18. SECURITY CLASSIFICATION OF THIS PAGE** Unclassified	**19. SECURITY CLASSIFICATION OF ABSTRACT** Unclassified	**20. LIMITATION OF ABSTRACT** UU

NSN 7540–01-280-5500 Standard Form 298 (Rev. 2–89)
Prescribed by ANSI Std. 239–18

THIS PAGE INTENTIONALLY LEFT BLANK

Approved for public release; distribution is unlimited

MEMS TERAHERTZ FOCAL PLANE ARRAY WITH OPTICAL READOUT

Hugo A. Gonzalez Jr.
Captain, United States Marine Corps
B.S., Florida International University, 2004

Submitted in partial fulfillment of the
requirements for the degree of

MASTER OF SCIENCE IN ASTRONAUTICAL ENGINEERING
AND
MASTER OF SCIENCE IN APPLIED PHYSICS

from the

NAVAL POSTGRADUATE SCHOOL
June 2016

Approved by: Gamani Karunasiri
Thesis Advisor

Fabio D. P. Alves
Co-Advisor

Jae Jun Kim
Second Reader

Kevin B. Smith
Chair, Department of Physics
Graduate School of Engineering and Applied Science

Garth V. Hobson
Chair, Department of Mechanical and Aerospace Engineering

THIS PAGE INTENTIONALLY LEFT BLANK

ABSTRACT

The terahertz (THz) spectral range remains a relatively untapped portion of the electromagnetic spectrum. THz radiation's unique ability to penetrate non-metallic materials presents an exciting opportunity for many imaging applications. The purpose of this research is to investigate a unique imaging method using a THz radiation source and metamaterial absorber. By using a metamaterial absorber, the THz detection frequency of interest can be tuned by controlling geometrical parameters with nearly 100% absorption. THz sensing can be achieved by integrating a metamaterial absorber with bi-material legs to form a sensor. Moveable mirror-like surfaces on the backside of the metamaterial under THz absorption can cause a deflection of visible light and from it, the original image can be reconstructed using an optical readout system. In this thesis, the construction of the optical readout system for characterization of sensor pixels as well as THz imaging is described.

THIS PAGE INTENTIONALLY LEFT BLANK

TABLE OF CONTENTS

LIST OF FIGURES

THIS PAGE INTENTIONALLY LEFT BLANK

LIST OF TABLES

THIS PAGE INTENTIONALLY LEFT BLANK

LIST OF ACRONYMS AND ABBREVIATIONS

AM	Amplitude Modulation
BFL	Back Focal Length
CCD	Charged Couple Device
CH-53E	USMC “Super Stallion” Heavy Lift Helicopter
FFL	Front Focal Length
FLIR	Forward Looking Infrared
FM	Frequency Modulation
FOV	Field of View
FPA	Focal Plane Array
FTIR	Fourier Transform Infrared
Gbps	Gigabits per second
GHz	Gigahertz
IR	Infrared
MEMS	Microelectromechanical Systems
QCL	Quantum Cascade Laser
MW-IR	Midwave Infrared
PW	Pulse Width
SRL	Sensor Research Laboratory
THz	Terahertz

THIS PAGE INTENTIONALLY LEFT BLANK

ACKNOWLEDGMENTS

First, I would like to thank the United States Marine Corps for giving me the opportunity and support to pursue a graduate education. I also would like to thank the faculty of the Naval Postgraduate School for imparting their knowledge that will carry me through all my future endeavors, and my friends and family for all their support. I am grateful to Fabio Alves and Gamani Karunasiri for their mentorship, friendship, and support, which made this body of work possible Finally, to my neighbors, Tim and Barbara, thank you for always watching over my dog, Rocky, while I was at school.

THIS PAGE INTENTIONALLY LEFT BLANK

I. INTRODUCTION

The terahertz (THz) spectral range forms a tiny part of the electromagnetic spectrum and has remained relatively unexploited until recently. This has been due in large part to the lack of sensitive sensors and powerful sources. The ability of THz radiation to penetrate most dielectric, non-metallic materials offers many applications. For security screenings [1], it is able to penetrate clothes and identify explosive materials. In the medical [2] field, THz radiation's non-ionizing characteristic allows it to be used for imaging applications while remaining safe for human exposure.

The Naval Postgraduate School's Sensor Research Laboratory (SRL) is currently conducting extensive research into THz imaging. The SRL has designed and fabricated highly tuned bi-material THz detectors as well as THz to IR converters using Microelectromechanical System (MEMS) technology.

The primary focus of this thesis is in the design and characterization of an optical readout system, which enables the use of visible or infrared light to probe an array of THz sensors for imaging.

Chapter II explains the principle of design and operation of the metamaterial THz detector and the optical readout setup.

Chapter III illustrates the modeling and simulation of a metamaterial-based THz-to-IR converter along with the characterization of the converter through key figures of merit.

Chapter IV details the experimental setup and results, which are compared to those obtained through simulation as well as a characterization of the optical readout.

Finally, concluding remarks with ideas for improving the optical readout are presented for potential future work.

A. BACKGROUND

Terahertz electromagnetic waves range from 0.3 – 10 THz (1000 - 30 μm) and form the “terahertz gap” sandwiched between infrared (IR) and microwaves (Figure 1).

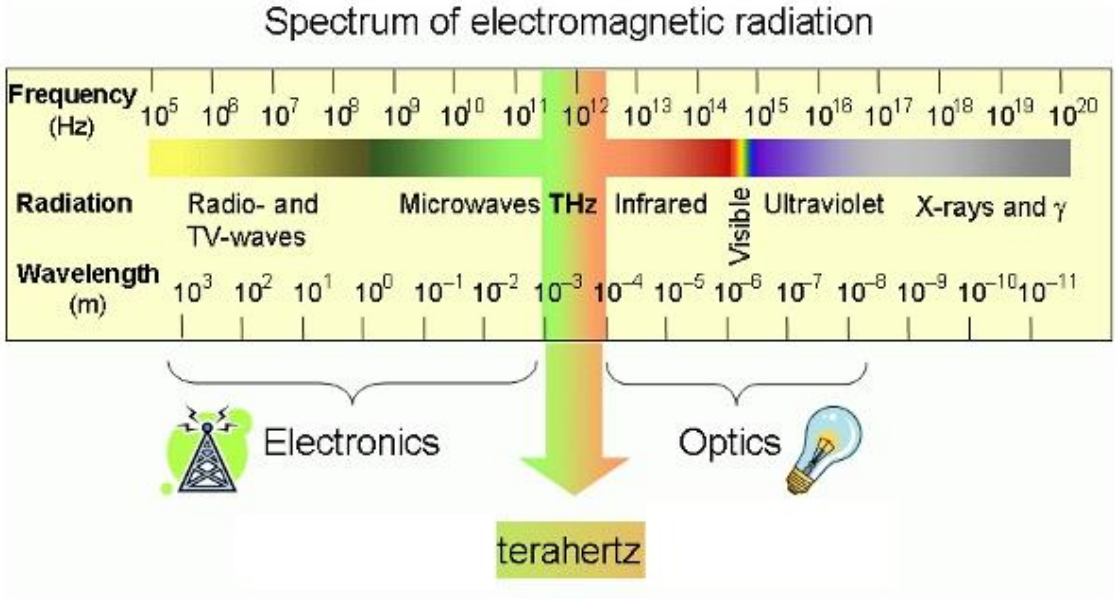

Figure 1. Electromagnetic Spectrum. Source: [3].

As Figure 1 also depicts, frequencies lower than terahertz (e.g., AM, FM, and microwave) are based on electronic generation and are governed by the world of electronics. In this region of the electromagnetic spectrum most dielectric materials are transparent which enables radio and cellular reception inside buildings. Frequencies higher than terahertz (infrared, visible, and ultraviolet) are based on quantum transitions and are governed by the world of optics. In this region, most materials are opaque and the waves easily scattered by dust, sand, fog, and other particulates suspended in air [4]. The shorter wavelengths associated with higher frequencies also results in higher resolution according to Rayleigh’s criteria:

$$\theta_r = 1.22\frac{\lambda}{D}\ , \tag{1}$$

where the angular resolution θ_r is directly dependent on the wavelength λ and dimension (D) of the aperture.

Having a much shorter wavelength than radio, microwave, or millimeter waves allows THz to provide a much greater resolution in imaging [4].

Since terahertz exists between IR and microwave, it can be generated using optical or electronic technology while also enjoying the benefits from each. Their ability to penetrate through many different materials that are opaque in the visible spectrum makes them extremely desirable for many applications [5]. Figure 2 shows that THz transmits through various types of clothing much better than IR.

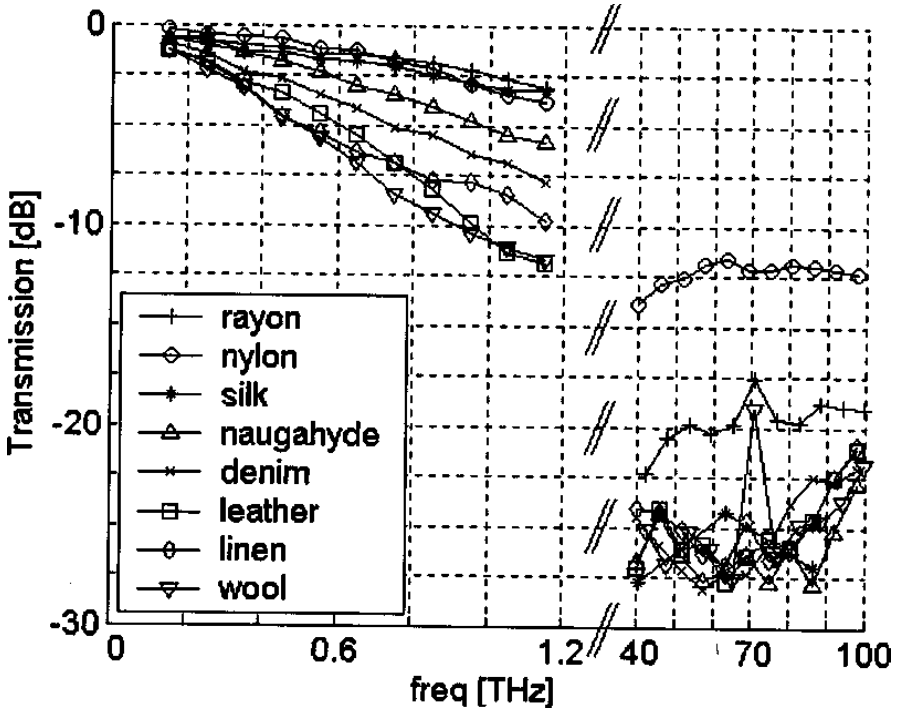

Figure 2. THz (Left) and MW-IR (Right) Transmission through Eight Clothing Samples. Source: [5].

B. SECURITY

Since THz radiation is easily transmitted through most dielectric materials, it can effectively pass through clothes, shoes, packaging, book bags, etc., allowing the identification and detection of potentially concealed weapons or explosives [1]. Since metals are highly reflective to THz, a weapon such as a knife or a gun could easily be recognized as shown in the cartoon representation of Figure 3.

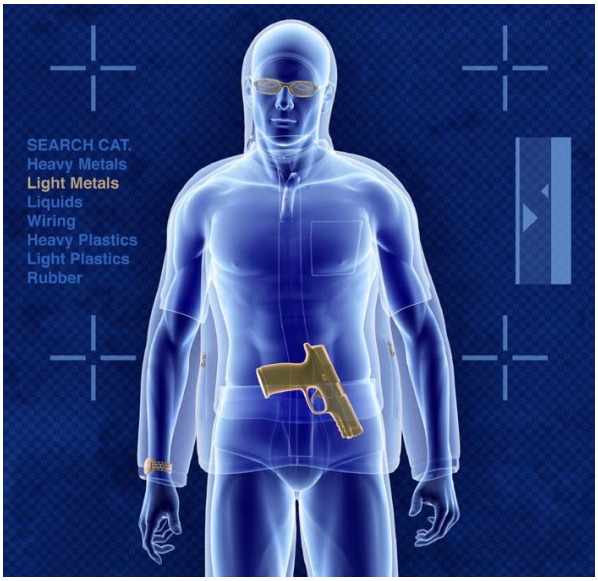

Figure 3. Graphic Depicting Potential THz Security Screening Application. Source: [5].

Due to THz's non-ionizing ability [2], it can safely pass through organic tissue without causing appreciable damage. Nearly all of the THz energy incident on a person would be absorbed by the high water content present in the skin. This would be harmlessly dissipated as heat within the first 100 μm of skin tissue [6]. This enables it to be used to scan individuals with a body scanner safely.

Currently airport security scanners use millimeter wave imaging operating at approximately 30 GHz (10 mm wavelength) [1]. Terahertz waves operating

between (0.3 – 10 THz) are capable of providing a spatial resolution 10 to 100 times greater than current security scanners according to Rayleigh's criteria (1).

Another unique feature of THz over millimeter waves is that many chemicals and biological agents have spectroscopic signatures in the THz range. As shown in Figure 4 many common explosives (e.g., C-4, HMX, RDX, and TNT) have characteristic transmission and reflection spectra that can be readily detected using THz [7].

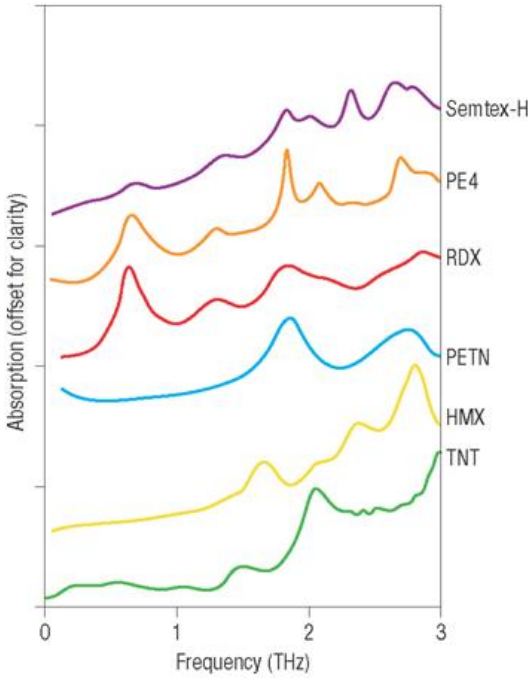

Figure 4. Characterization of Common Explosives with Unique THz Spectral Fingerprints. Source [8].

C. MEDICAL

Due to its non-ionizing characteristics, THz can provide highly detailed medical imaging such as tracking cancer progression and wound healing assessment [2]. Skin and breast cancer detection have already been successfully demonstrated [7], [9].

In dental applications, it has been found that mineral loss in enamel (a precursor to cavities) can be detected by using THz and analyzing the change in refractive index of the enamel. Using this method cavities can be spotted much sooner than by using X-rays [9], Figure 5.

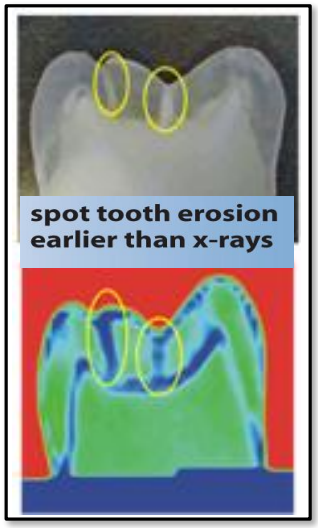

Figure 5. By Analyzing the Change in Refractive Index of Enamel THz Can Detect Cavities Sooner. Tooth Erosion Imaged with X-Rays (Top) and THz (Bottom). Source [10].

D. COMMUNICATIONS

With the ever-growing demand for wireless communications, it is estimated that data rates of 5–10 Gbps will be required by 2020. With THz's inherent larger bandwidth, a tremendous amount of research is being conducted on communication systems using sub-THz to THz frequencies (0.1 – 2 THz) [11].

THz promises data rates of at least 100 Gbps and some predict that Wi-Fi will be replaced with a THz based system by the year 2023 [11].

E. SEEING THROUGH ATMOSPHERIC PARTICULATES

Figure 6 shows a “brown-out’ in which a helicopter lands in a dusty landing zone and visibility is severely reduced due to the blowing sand. A promising solution could be THz’s is the ability to see through atmospheric particulates thereby allowing the pilots to maintain reference with the ground.

Figure 6. CH-53E Experiencing a “Brown-Out” in Afghanistan.

In order to determine if sand is transparent to THz imaging one needs to examine scattering ability of a sand grain. The less a particle scatters light the more transparent it is. There are three principal types of scattering that can be identified by first determining the ratio:

$$x = \frac{2\pi r}{\lambda} \ , \tag{2}$$

where x is a dimensionless size parameter, r represents the spherical particle radius, and λ is the wavelength.

If x is much less than 1, it will result in Rayleigh scattering, if it is approximately equal to 1 it results in Mie scattering, and if it is much greater than 1 it results in Geometric Scattering [12]. Figure 7 shows the typical sand particle size for a sample taken from Afghanistan. One can see that most particles are

between 10 μm and 500 μm in size. Highlighted is the THz range, which is capable of minimal scattering for particles less than 1–10 microns in size depending on which end of the THz spectrum one employs.

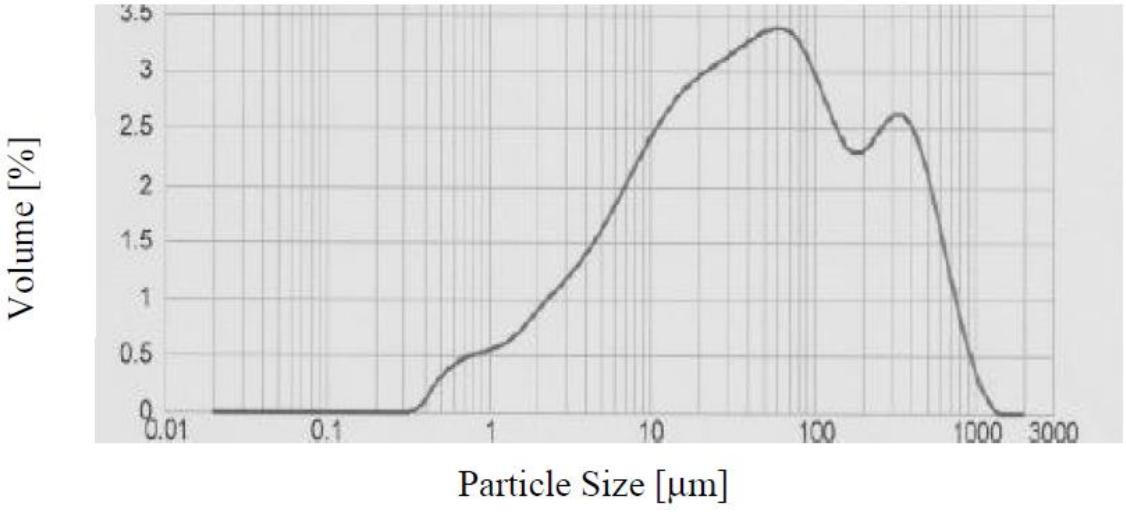

Figure 7. Sand Particle Size Distribution for a Sample from Afghanistan. Source: [13].

II. METAMATERIAL MEMS SENSOR READOUT

A. TERAHERTZ DETECTION

The amount of THz energy at room temperature is illustrated in the blackbody diagram in Figure 8. At room temperature there is much less THz than IR energy that most objects must be illuminated with a THz source to allow detection.

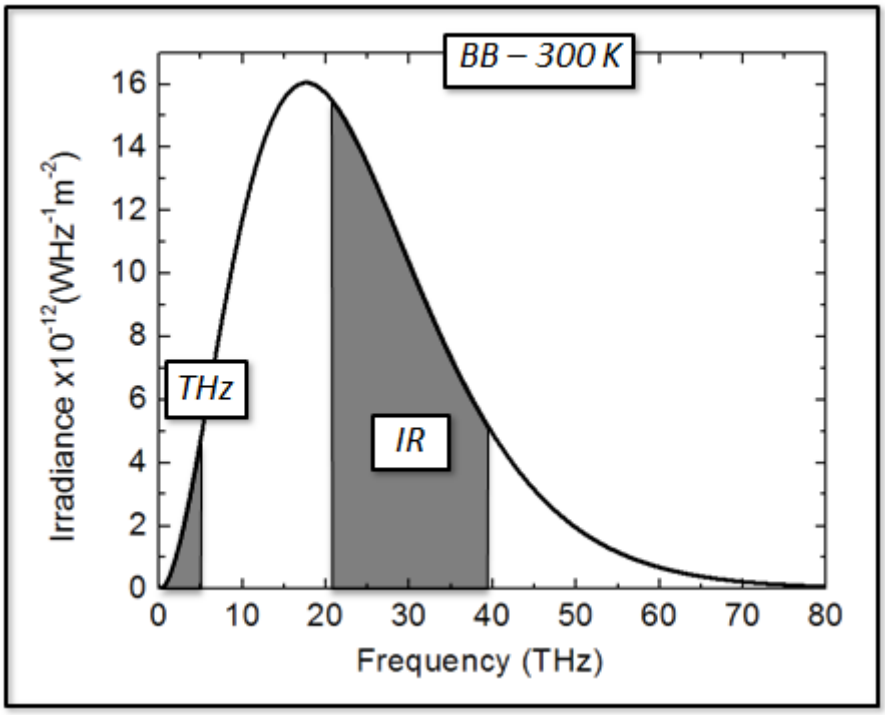

Figure 8. 300k Blackbody Radiation Illustrates the Small Amount of THz Energy Present at Room Temperature Compared to IR Energy. Source: [14].

Two modes of illumination can be employed, transmission and reflection. In transmission, an object is placed between the source and sensor and an image is formed by radiation that is transmitted through the object. In reflection, the source and sensor are displaced by the same angular separation from the object and an image is formed by radiation that is reflected off the object (Figure

9). In this research, transmission was employed due to easier setup when compared with reflection mode.

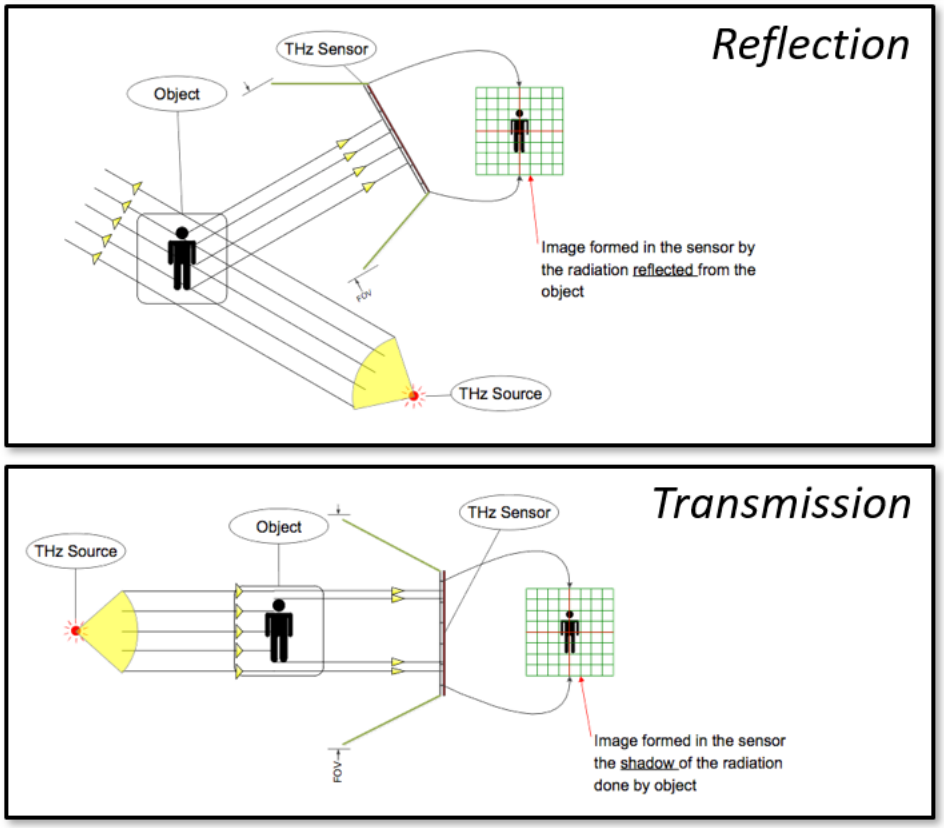

Figure 9. Illumination of an Object via Reflection (Top) and Transmission (Bottom). Source: [14].

In order to make a detector sensitive to the THz frequencies of interest a metamaterial absorber was employed. It consists of a silicon dioxide layer sandwiched by a homogeneous aluminum film (ground plane) and a periodic array of aluminum square elements as shown in Figure 10.

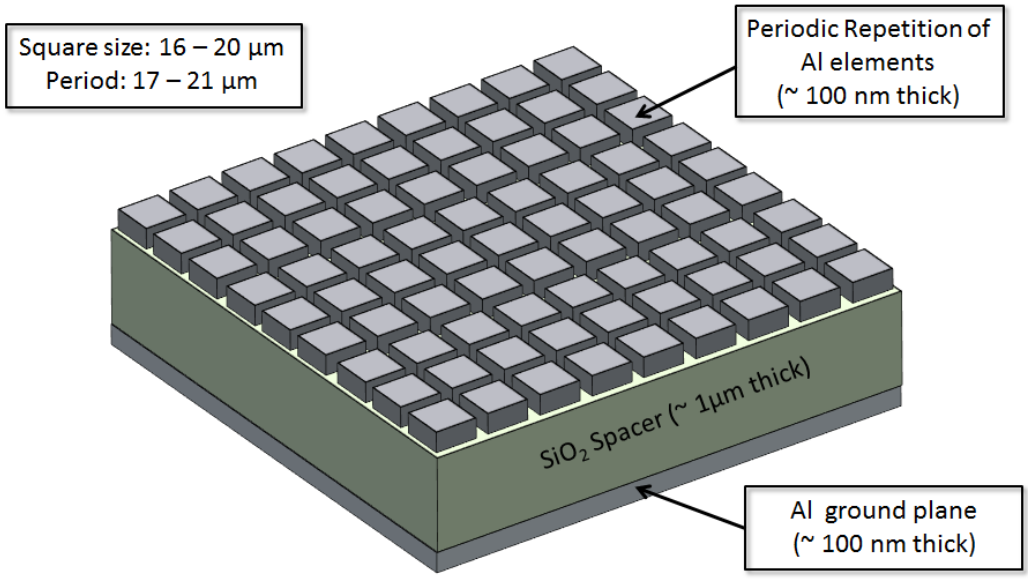

Figure 10. THz Metamaterial Absorber that can be Tuned to a Particular Frequency by Varying the Square Elements' Dimensions. Source: [14].

By varying the dimensions of the square elements, one can tune the metamaterial to a particular frequency. Fourier transform infrared spectroscopy (FTIR) corroborated the results from Finite Element Simulations that showed as the dimensions of the square elements are reduced, the frequency of peak absorption is increased (Figure 11). In the Sensor Research Laboratory, the available THz source is a 3.78 THz Quantum Cascade Laser, therefore the appropriate square size to maximize absorption would be 18 µm.

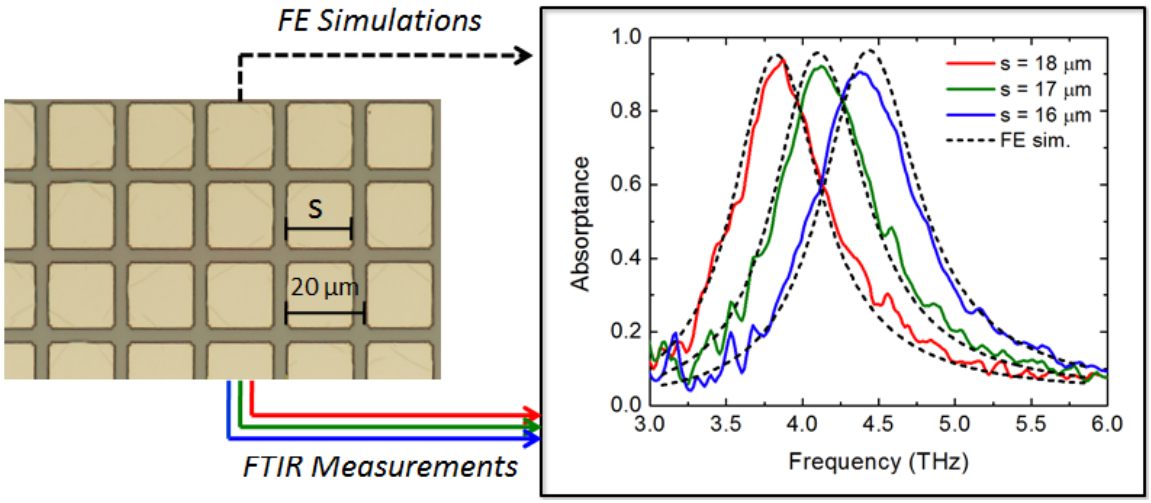

Figure 11. Dimensions of Periodic Square Elements (Left). Finite Element Simulation of Maximum Frequency Absorption for Different Periodic Square Dimensions Closely Resembles Actual FTIR Measurements (Right). Source: [14].

The metamaterial absorber was integrated with a bi-material MEMS sensor to allow transduction of the absorbed THz energy into angular displacement. In the bi-material sensor, the metamaterial absorber is attached to a silicon heat sink via a thermal insulator (pure SiO_2) and two bi-material legs formed by Al and SiO_2 as shown in Figure 12.

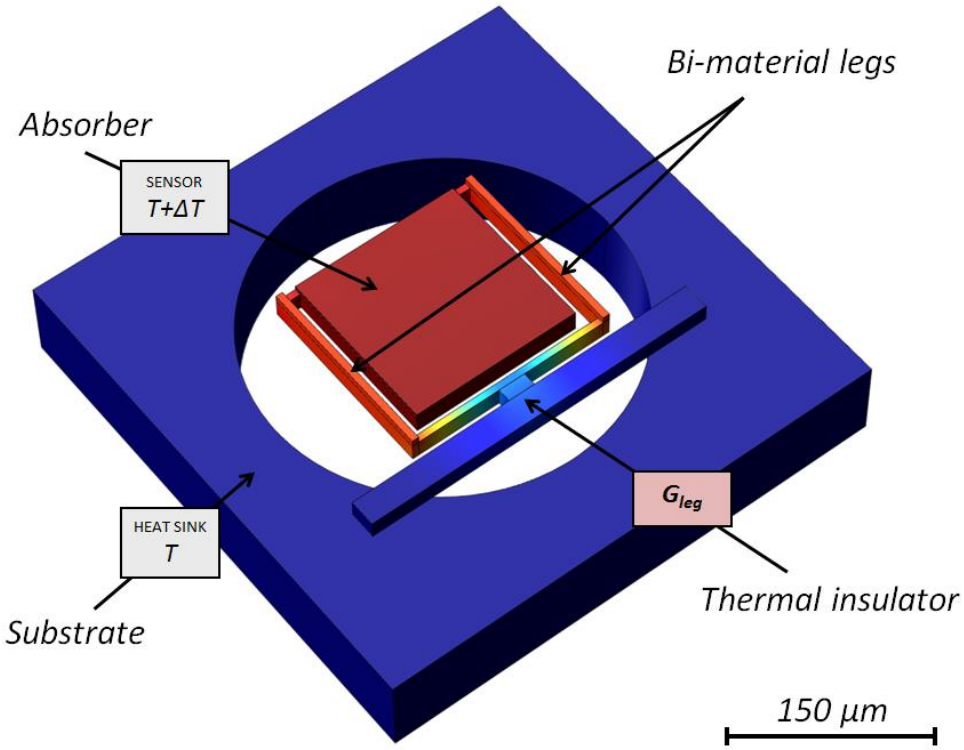

Figure 12. THz Metamaterial Absorber. Source: [14].

The bi-material sensor operates as follows: as the metamaterial absorbs THz energy, it heats up and the heat is transferred to the bi-material legs. The thermal insulator, which connects the bi-material legs to the heat sink, keeps the heat on the bi-material legs long enough for them to undergo deformation.

Two important figures of merit of the sensor are the thermal time constant:

$$\tau = \frac{C}{G} \ , \tag{3}$$

where C is the heat capacitance and G is the thermal conductance and the responsivity:

$$\Re = \frac{\eta}{G}\frac{\Delta\theta}{\Delta T} \ , \tag{4}$$

where η is the absorption efficiency, $\Delta\theta$ is the angular deflection of the sensor, and ΔT is the change in temperature of the sensor.

The “thermal time constant” is used to determine the maximum speed of operation. It is directly proportional to the heat capacitance but inversely proportional to the thermal conductance. The thermal conductance in the bi-metallic sensor can be increased by increasing the contact area with the thermal insulator thereby increasing the thermal heat flux to the heat sink.

Responsivity measures how much angular deflection in the sensor is obtained for a given incident power. It is also inversely proportional to the thermal conductance.

The higher the thermal conductance the faster the sensor can dissipate heat, which results in an increase in the thermal bandwidth of the sensor. However, as the thermal conductance increases, the responsivity will decrease making it more difficult to detect a small change in temperature.

Figure 13, illustrates the simulated response of three sensor configurations with different thermal conductance, from “C” being the highest to “A” being the lowest, to a THz laser square pulse.

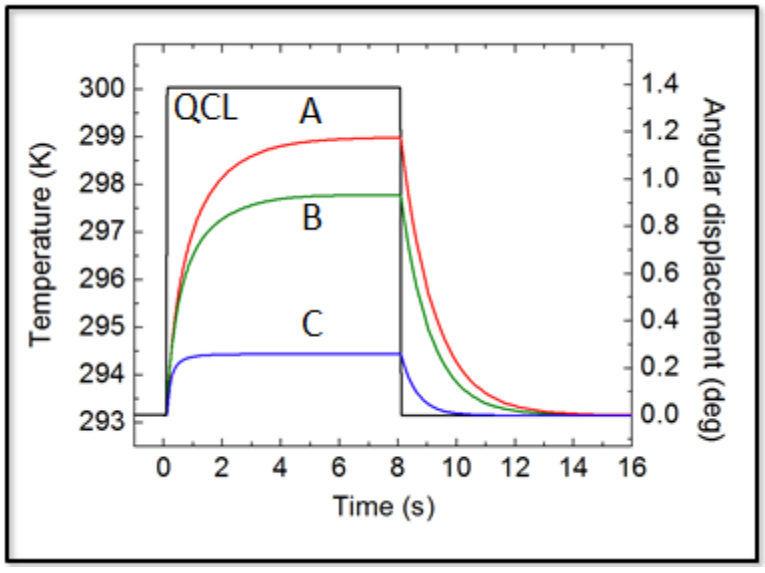

Figure 13. Simulated Response of Three THz Sensor Configurations to a THz Laser Square Pulse. Thermal Conductance from Lowest to Highest: A, B, C. Source: [14].

Configuration A shows the largest angular deflection for a given amount of incident power but has the slowest operation speed taking approximately four seconds to reach its peak temperature and another four seconds to dissipate it. Configuration C has the smallest angular deflection but the fastest speed of operation taking less than a second to saturate and less than two seconds to dissipate all its thermal energy.

B. IMAGING WITH THE FOCAL PLANE ARRAY

Using MEMS fabrication technology, an array of these sensors (known as the focal plane array) is formed on a silicon wafer. If an object to be image is placed between the THz source and the front side of the FPA then it will transmit varying intensity levels of THz to each individual sensor. On the back side of each sensor is a layer of aluminum, which acts like a mirror for visible light. A close-up of the back side of the FPA is shown in Figure 14.

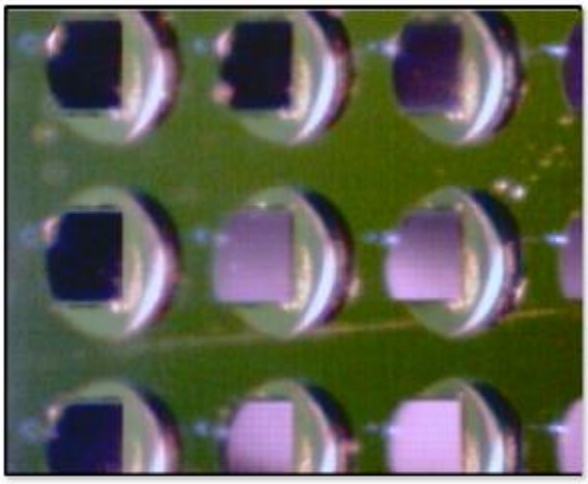

Figure 14. Mirror-Like Back Side of Each Pixel. Source: [14].

The greater the amount of THz energy incident on each detector, the larger the deflection of each mirror. If one were to shine light on the back of the FPA, it is possible to correlate the intensity of the reflected light with the deflection angle of each mirror using specific optical arrangements. A zero

deflection angle would correspond to maximum brightness, and as the deflection angle is increased, the brightness would decrease until a certain critical angle was reached.

Each sensor (also referred to as a pixel) on the focal plane array has a dimension of 380 µm x 380 µm. Figure 15 shows a square detector of 50 x 50 pixels with outer dimensions of 19 mm x 19 mm.

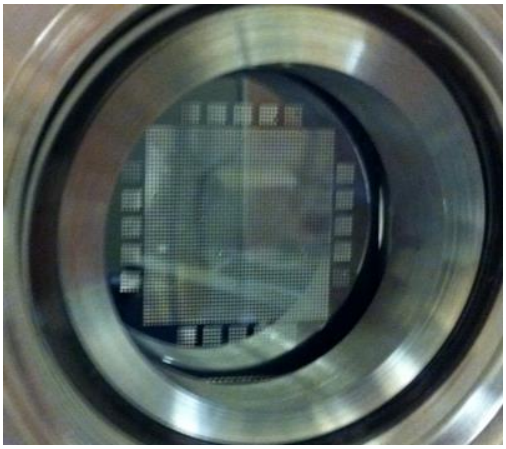

Figure 15. 3.8 THz Focal Plane Array Mounted in a Vacuum Cell.

C. OPTICAL READOUT SETUP

A schematic of the quantum cascade laser and focal plane array along with the optical readout system (outlined in red) is shown in Figure 16.

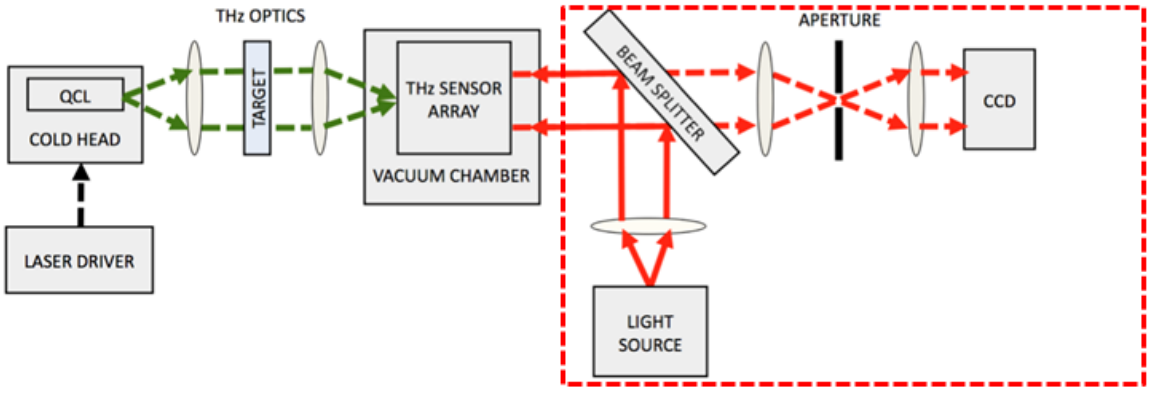

Figure 16. QCL and Optical Readout System Schematic.

The method of operation is as follows:

1. QCL illuminates the target
2. Transmitted THz energy from the target is focused onto the FPA
3. Individual sensors deflect (proportional to incident energy)
4. A collimated light source is directed onto a beam splitter which shines the back side of the FPA
5. Light reflects from the back of the sensors and passes through the beam splitter towards the primary lens
6. Primary lens focuses reflected light on to an aperture
7. Secondary lens re-collimates the light rays to be imaged by a CCD camera

The light source selected was a 520 nm green light emitting diode. A single color was selected to minimize chromatic aberrations that would occur within the optical system if white light were used. A secondary advantage is that the CCD camera is highly sensitive to green light.

A 50/50 beamsplitter was selected in order to easily redirect the collimated light source on to the back of the focal plane array. It does this by allowing 50% of the light source to reflect towards the FPA while the 50% is transmitted through. Then 50% of the light coming off the FPA is reflected towards the source while the other 50% is transmitted through the optical system. The net result is that 25% of the original light intensity is transmitted throughout the system and needs to be taken into account when selecting a light source.

The light then passes through the primary lens to be focused at the aperture. An achromatic doublet was used in order to minimize spherical aberrations. The primary lens focuses the light onto an aperture located at the back focal length of the lens. A 150 μm aperture was used to reduce the intensity of deflected light rays from the FPA thereby increasing the contrast of those areas on the FPA that absorb THz energy.

Finally, the secondary lens re-collimates the light to be imaged by the CCD camera. Collimation was used not only to focus the image onto the CCD detector but also to eliminate distortions such as the pincushion or barrel effect associated with non-collimated light.

In order to obtained a collimated output beam for the CCD camera one could as a rough estimation use the thin-lens combined focal length equation:

$$\frac{1}{f} = \frac{1}{f_1} + \frac{1}{f_2} - \frac{d}{f_1 f_2} \tag{5}$$

Since we want a collimated beam as the output this means the equivalent focal length goes to infinity and hence:

$$\frac{1}{\infty} = \frac{1}{f_1} + \frac{1}{f_2} - \frac{d}{f_1 f_2} \Leftrightarrow \frac{d}{f_1 f_2} = \frac{1}{f_1} + \frac{1}{f_2} \tag{6}$$

$$d = f_1 + f_2 \tag{7}$$

Since $f_1 = 75\,mm$ and $f_2 = 25\,mm$ we have:

$$d = 75 + 25 = 100\,mm \tag{8}$$

However, as discussed previously, equation (5) is only applicable to thin lenses. With the primary and secondary lenses having thicknesses of 23 mm and 10 mm respectively (approximately equal to their radius) they are anything but thin. For these lenses, we need to look up their specifications [Appendix A] and model them using the optical matrix method. The advantage of this method is twofold: first, we can account for the thickness of the lens and secondly a more accurate solution can be obtained using the precise index of refraction for a specific wavelength, for the green LED $\lambda = 520\,nm$.

The primary doublet lens is made of two different pieces of glass (E-BAF11 and N-SF11) which are cemented together. The respective indices of refraction and dimensions are as follows:

Table 1. Specifications for Primary Achromatic Doublet Lens.

n_1 (E-BAF11)	Index of refraction of E-BAF11 glass	1.6725
n_2 (N-SF11)	Index of refraction of N-SF11 glass	1.7975
t_1 (E-BAF11)	Thickness of E-BAF11 glass	20 mm
t_2 (N-SF11)	Thickness of N-SF11 glass	3 mm
R_1	Curvature radius of front (input) side	50.8 mm
R_2	Curvature radius of middle glass interface	-41.7 mm
R_3	Curvature radius of back (output) side	-247.7 mm

*Where (-) represents a concave surface.

Given the dimensions, the matrix method yields the following:

$$M_1 = \begin{pmatrix} 1 & 0 \\ \frac{1}{R_3}(n_2\text{-}1) & n_2 \end{pmatrix}\begin{pmatrix} 1 & t_2 \\ 0 & 1 \end{pmatrix}\begin{pmatrix} 1 & 0 \\ \frac{1}{R_2}(\frac{n_1}{n_2}\text{-}1) & \frac{n_1}{n_2} \end{pmatrix}\begin{pmatrix} 1 & t_1 \\ 0 & 1 \end{pmatrix}\begin{pmatrix} 1 & 0 \\ \frac{1}{R_1}(\frac{1}{n_1}\text{-}1) & \frac{1}{n_1} \end{pmatrix} \quad (9)$$

$$M_1 = \begin{pmatrix} A & B \\ C & D \end{pmatrix} = \begin{pmatrix} 0.8238 & 13.6870 \\ -0.0134 & 0.9918 \end{pmatrix} \quad (10)$$

From which we can determine the focal lengths and primary planes as follows:

$$f_1 = \frac{1}{C} = -74.8\,mm \quad (11)$$

$$f_2 = -\frac{1}{C} = 74.8\,mm \quad (12)$$

$$H_1 = r = \frac{D-1}{C} = 0.62\,mm \tag{13}$$

$$H_2 = s = \frac{1-A}{C} = -13.18\,mm \tag{14}$$

$$FFL = f_1 + H_1 = -74.19\,mm \tag{15}$$

$$BFL = f_2 + H_2 = 61.63\,mm \tag{16}$$

The front focal length (FFL) measured from the left vertex lies 74.19 mm to the left and the back focal length (BFL) measured from the right vertex lies 61.63 mm. The BFL is critical because this is where we will locate the aperture.

The secondary biconvex lens is made of a single piece of glass (N-BK7) The respective index of refraction and dimensions are as follows:

Table 2. Specifications for Secondary Biconvex Lens.

n_1 (N-BK7)	Index of refraction of E-BAF11 glass	1.5168
t_1 (N-BK7)	Thickness of E-BAF11 glass	10.1 mm
R_1	Curvature radius of front (input) side	24.397 mm
R_2	Curvature radius of back (output) side	-24.397 mm

*Where (-) represents a concave surface as per the standard convention.

The matrix method yields:

$$M_2 = \begin{pmatrix} 1 & 0 \\ \frac{1}{R_2}(n_1\text{-}1) & n_1 \end{pmatrix} \begin{pmatrix} 1 & t_1 \\ 0 & 1 \end{pmatrix} \begin{pmatrix} 1 & 0 \\ \frac{1}{R_1}(\frac{1}{n_1}\text{-}1) & \frac{1}{n_1} \end{pmatrix} \tag{17}$$

$$M_2 = \begin{pmatrix} A & B \\ C & D \end{pmatrix} = \begin{pmatrix} 0.8585 & 6.6799 \\ -0.0394 & 0.8585 \end{pmatrix} \tag{18}$$

From which we can determine the focal lengths and primary planes as follows:

$$f_1 = \frac{1}{C} = -25.4\,mm \tag{19}$$

$$f_2 = -\frac{1}{C} = 25.4\,mm \tag{20}$$

$$H_1 = r = \frac{D-1}{C} = 3.59\,mm \tag{21}$$

$$H_2 = s = \frac{1-A}{C} = -3.59\,mm \tag{22}$$

$$FFL = f_1 + H_1 = -21.81\,mm \tag{23}$$

$$BFL = f_2 + H_2 = 21.81\,mm \tag{24}$$

Both the front and back focal lengths lie 21.81 mm from the left and right vertices, respectively.

In order to find the exact distance required between both lenses that results in parallel light rays the total system is modeled as follows:

$$M_T = M_2 \begin{pmatrix} 1 & d \\ 0 & 1 \end{pmatrix} M_1 \tag{25}$$

Where d is the distance between both lenses and we obtain:

$$M_T = \begin{pmatrix} A & B \\ C & D \end{pmatrix} = \begin{pmatrix} A_{M_2}(A_{M_1} + dC_{M_1}) + B_{M_2}C_{M_1} & A_{M_2}(B_{M_1} + dD_{M_1}) + B_{M_2}D_{M_1} \\ C_{M_2}(A_{M_1} + dC_{M_1}) + D_{M_2}C_{M_1} & C_{M_2}(B_{M_1} + dD_{M_1}) + D_{M_2}D_{M_1} \end{pmatrix} \tag{26}$$

Recall that for the matrix method the input and output ray heights and angles are given by:

$$\begin{pmatrix} y_f \\ \alpha_f \end{pmatrix} = \begin{pmatrix} A & B \\ C & D \end{pmatrix} \begin{pmatrix} y_0 \\ \alpha_0 \end{pmatrix}, \tag{27}$$

which is equivalent in algebraic form

$$\begin{aligned} y_f &= Ay_0 + B\alpha_0 \\ \alpha_f &= Cy_0 + D\alpha_0 \end{aligned} \tag{28}$$

Setting $C_{M_T} = 0$ defines a telescoping system in which parallel input rays produce parallel output rays ($\alpha_f = D\alpha_0$).

$$C_{M_T} = 0 = C_{M_2}(A_{M_1} + dC_{M_1}) + D_{M_2}C_{M_1} \tag{29}$$

Solving for d:

$$d = (-\frac{D_{M_2}C_{M_1}}{C_{M_2}} - A_{M_1}) / C_{M_1} \Leftrightarrow d = 83.43\,mm \tag{30}$$

This means the left vertex of the secondary lens must be placed 83.43mm from the right vertex of the primary lens (or 21.8mm from the aperture which is at the BFL) in order to recollimate the beam.

The magnification m of a telescopic system is:

$$m = -\frac{f_{\text{sec}}}{f_{\text{pri}}} \tag{31}$$

$$m = -\frac{25.4\,mm}{74.8\,mm} = -0.3396 \tag{32}$$

Hence, the resulting image is inverted and demagnified by a factor of 0.3396.

The camera used is a Basler A631f with a resolution of 1040 x 1392 pixels. Each pixel has a size of 4.65 μm x 4.65 μm, which results in overall CCD dimensions of 4.836 mm x 6.473 mm. The required demagnification in both length and height can be found using the dimensions of the FPA (19 mm x 19 mm):

$$\begin{aligned} m_l &= \frac{6.473\,mm}{19\,mm} = 0.341 \\ m_h &= \frac{4.836\,mm}{19\,mm} = 0.255 \end{aligned} \tag{33}$$

The current demagnification is slightly less than what is required and will result in a small portion being clipped off. In order to capture the entire focal plane array the optical system would have to be designed to a demagnification of 0.255. Referencing eq. (31) this can be achieved by either using a primary lens with a longer focal length or a secondary lens with a shorter focal length. For instance having a primary lens with a focal length of 100mm results in a magnification of

$$m = -\frac{25.4\,mm}{100\,mm} = -0.254\ , \tag{34}$$

which would allow the imaging of the entire FPA. Conversely, a higher resolution camera with a larger CCD array would also be able to image the entire FPA.

As Figure 17 shows, it can be assumed that as each individual pixel on the FPA deflects light, it will be swept across the aperture. As the beam width of the light approaches the edge of the aperture, more of it becomes blocked and the intensity is reduced until the light is completely blocked.

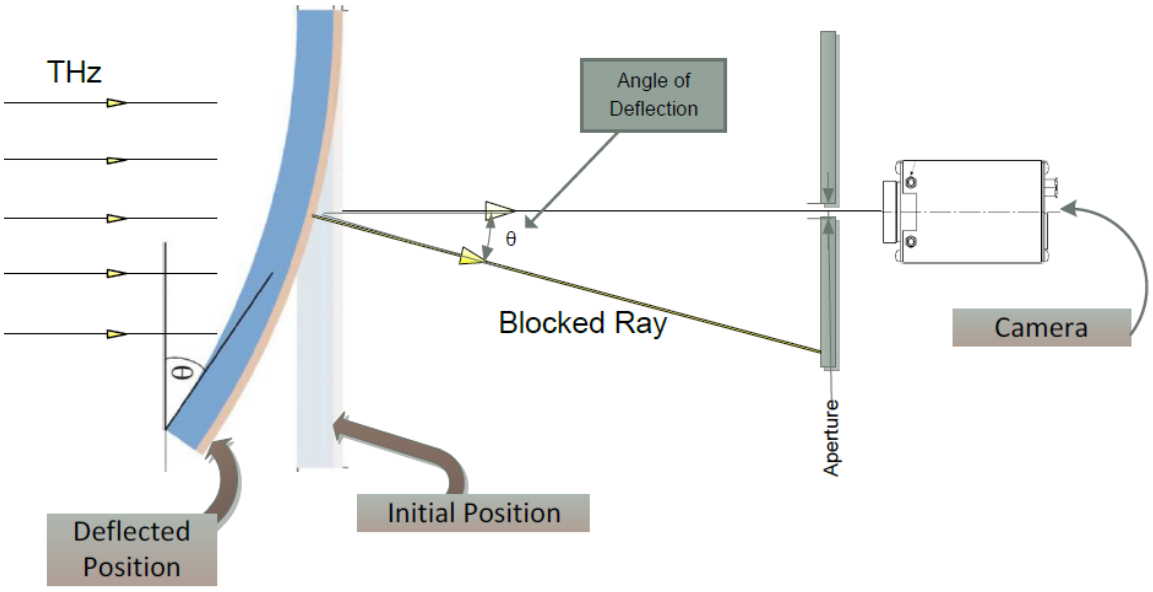

Figure 17. Angular Deflection of Sensor Causes Light to be Swept Across the Aperture. Source: [15]

As a first order approximation, it can be assumed that light needs to traverse a displacement equivalent to the size of the aperture at the focal point of the primary lens to go from a maximum to minimum intensity.

Due to the flexural stress present on the metamaterial absorber, each pixel on the FPA can be modeled as a convex mirror with a 2 mm center of curvature and a diameter of 200 μm. This yields a matrix equivalent to:

$$M_3 = \begin{pmatrix} 1 & 0 \\ \frac{1}{2\,mm} & 1 \end{pmatrix} \tag{35}$$

The maximum deflection will occur for a light ray at approaching the mirror near its outer edge at height of 100 μm. Given the distance of the FPA from the primary lens as 180 mm, the system matrix can be modeled as:

$$\begin{pmatrix} y_f \\ \alpha_f \end{pmatrix} = \begin{pmatrix} 1 & f_1 \\ 0 & 1 \end{pmatrix} M_1 \begin{pmatrix} 1 & s \\ 0 & 1 \end{pmatrix} [\begin{pmatrix} 0 \\ \theta \end{pmatrix} + M_3 \begin{pmatrix} y_0 \\ \alpha_0 \end{pmatrix}] \tag{36}$$

With the following conditions:

$$y_0 = 100\,mm$$
$$\alpha_0 = 0^o$$
$$s = 180\,mm$$
$$y_f = 150\,\mu m$$

When solved for θ it results in a value of $\theta = 2.98^o$. This represents the maximum deflection required to change the intensity of the optical readout from a minimum to a maximum.

III. MODELING AND SIMULATION OF A METAMATERIAL BASED THZ TO IR CONVERTER

A. SENSOR DESCRIPTION

The bi-material THz sensor is well studied and simulations and measurement results can be found in [16]. The THz to IR conversion is a relatively new concept and a characteristics of its responses is necessary to design a proper IR readout scheme. The THz-to-IR converter allows for the direct conversion of THz to IR energy, which can be read using a commercial off the shelf (COTS) FLIR camera leveraging an inexpensive and reliable technology. The primary advantage of the THz-to-IR converter over the bi-material THz sensor is that by replacing the two bi-material legs with a four-legged SiO_x bridge, many of the deformations inherit in the bi-material sensor are avoided.

A secondary advantage of the THz-to-IR converter is that it can be fabricated with SU-8 thereby reducing steps in the MEMS fabrication process. The dimensions of the metamaterial surface area of a pixel is 200 µm x 200 µm while the FPA pitch area is 312 µm x 312 µm.

B. SENSOR DESCRIPTION

Modeling and simulation of THz-to-IR conversion was done using COMSOL while MATLAB was used to analyze the results. The COMSOL model of a single sensor on the FPA is shown in Figure 18.

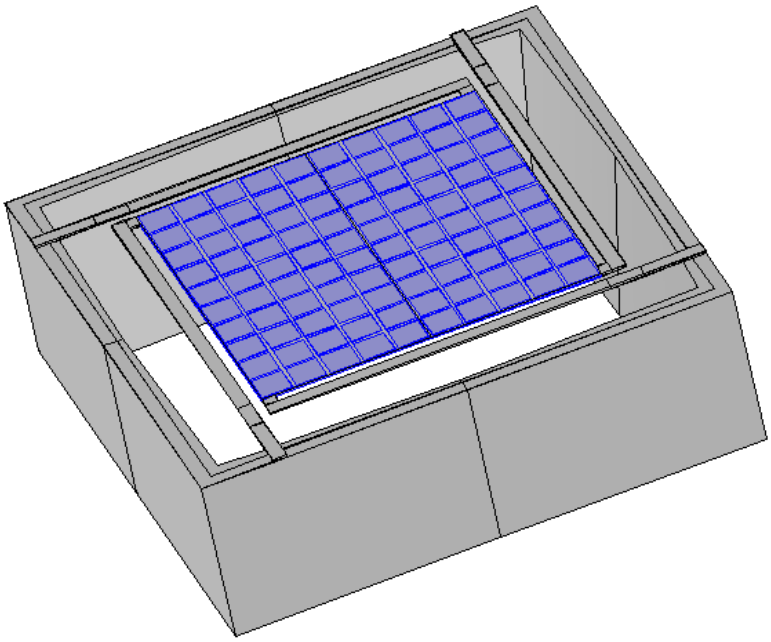

Figure 18. COMSOL THz-to-IR Converter Model. Metamaterial Surface Area (Purple): 200 µm X 200 µm. Individual Pixel Area (Including the Outer Substrate): 312 µm X 312 µm.

COMSOL's heat transfer module was used to characterize the sensor as the QCL's frequency and power were varied.

C. QCL POWER

Power reaching the absorber of a single sensor was measured for the experimental setup used and found to be around 1 µW. This occurred when the laser was operated at f = 10 kHz with a pulse width (PW) of 5 µs (maximum power) using:

$$P_{peak} = \frac{P_{avg}}{DutyCycle} \ , \tag{37}$$

where P_{peak} is the maximum peak power, P_{avg} is the average power during one waveform period, and $DutyCycle$ is the percentage of time the laser is on and is given as

$$DutyCycle = \frac{PW}{1/f} = f \times PW \ , \tag{38}$$

P_{peak} was found to be 20 μW. The relationship between the operating frequency and average power is then given by:

$$P_{avg} = P_{peak} \times PW \times f \tag{39}$$

Since P_{peak} is invariable and keeping PW fixed at 5μs,

$$P_{avg} = f \times 10^{-10} \tag{40}$$

D. POWER RESPONSE

Assuming that absorption efficiency is 100% (metamaterial is a perfect absorber), the average power from the QCL reaching the detector is also the total heat flux through the sensor.

The simulation was performed setting a constant heat flux through the boundary representing the front of the sensor and recording the change in temperature on the back surface as a function of time. Figure 18 shows the temperature distribution on the back surface when steady state is achieved.

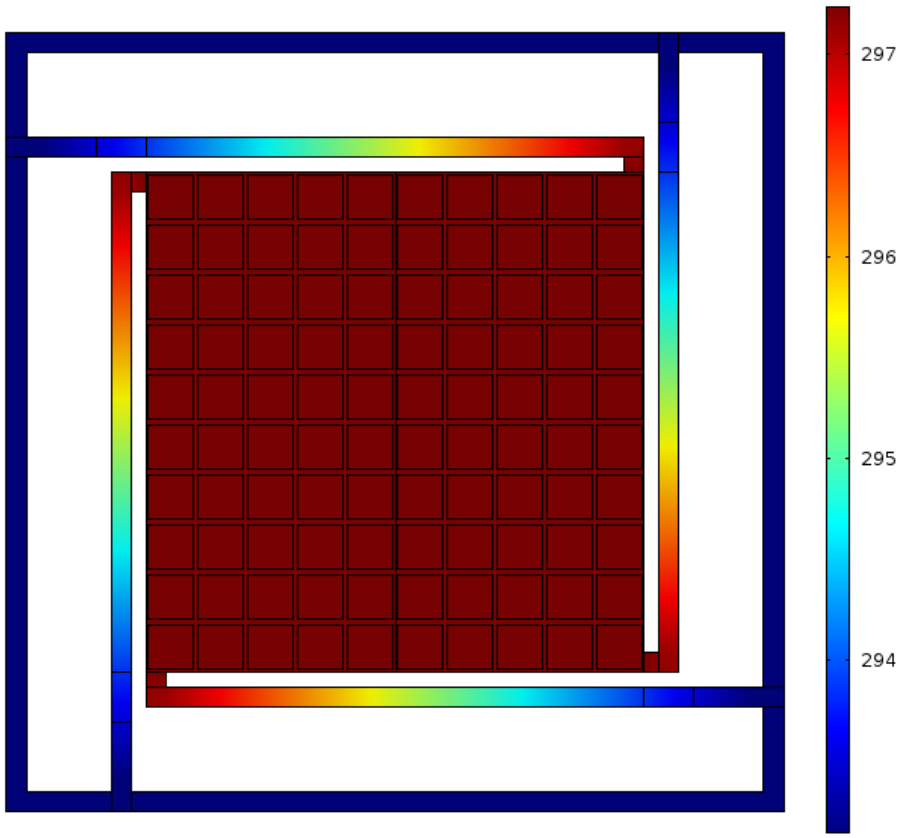

Figure 19. THz-to-IR Sensor Heat Transfer from Heat Flux Simulation.

To determine the power response a parametric sweep of the heat flux was varied from 0.1 µW to 1 µW. The time domain responses for incident power levels of 0.1 µW and 1 µW are shown in Figure 20.

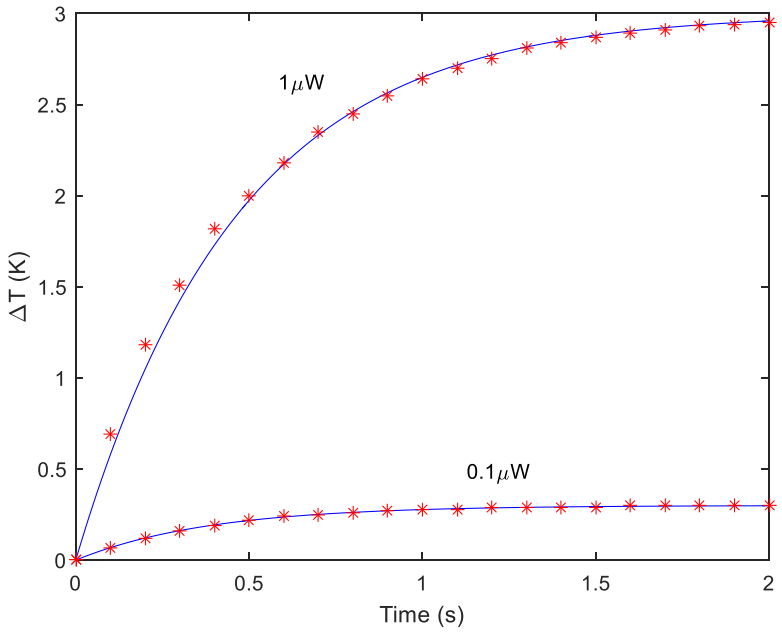

Figure 20. Time Domain Response for 0.1 µW and 1 µW Incident Laser Power.

As expected, the change in temperature varies proportionally to the incident QCL power and the correlation is highly linear, as can be seen in Figure 21.

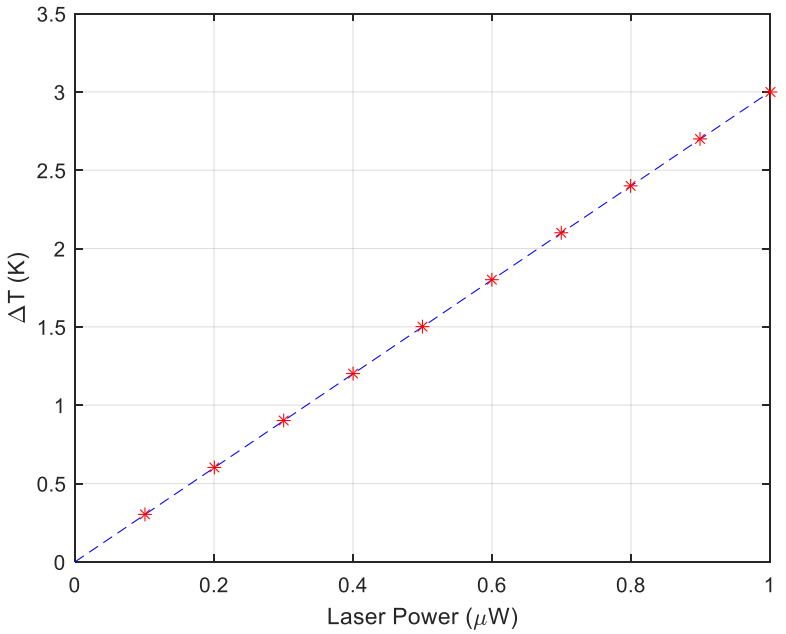

Figure 21. Temperature Change as a Function of Incident THz Power When the Sensor is Gated at 0.5 Hz.

E. FREQUENCY RESPONSE

In order to obtain the frequency response the QCL gating, waveform was modeled as a binary square wave with gating frequency f_g. The maximum QCL power incident on the absorber area of one pixel (1 μW) was multiplied by this square wave to simulate the on-off behavior of the gated QCL being used in actuality.

A time domain simulation with a parametric sweep of the gating frequency from 0.1 Hz to 10 Hz was conducted. The speed of operation is dependent on the thermal time constant of the sensor ($\tau = C/G$) as previously discussed. As the frequency of the gated pulse increases, the less time the sensor has to capture power from the laser and hence the amount of temperature change as seen in the plots for 0.1 Hz and 10 Hz (Figures 22 and 23).

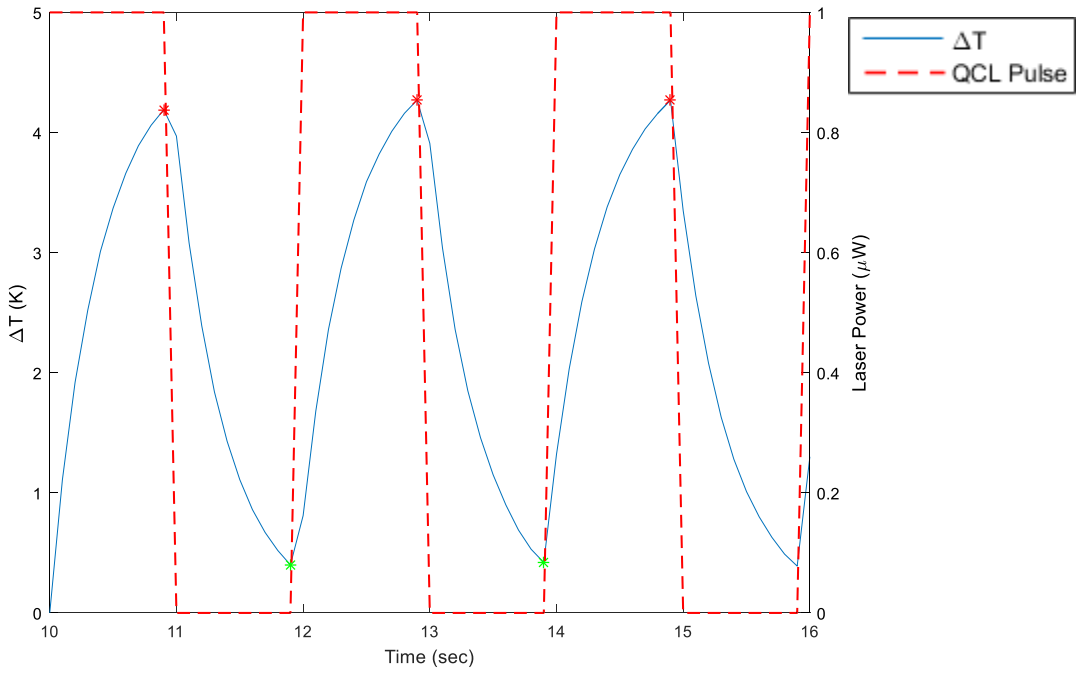

Figure 22. Time Domain Response for One Sensor Under Illumination of 1 μW Incident Laser Power Gated at 0.5 Hz.

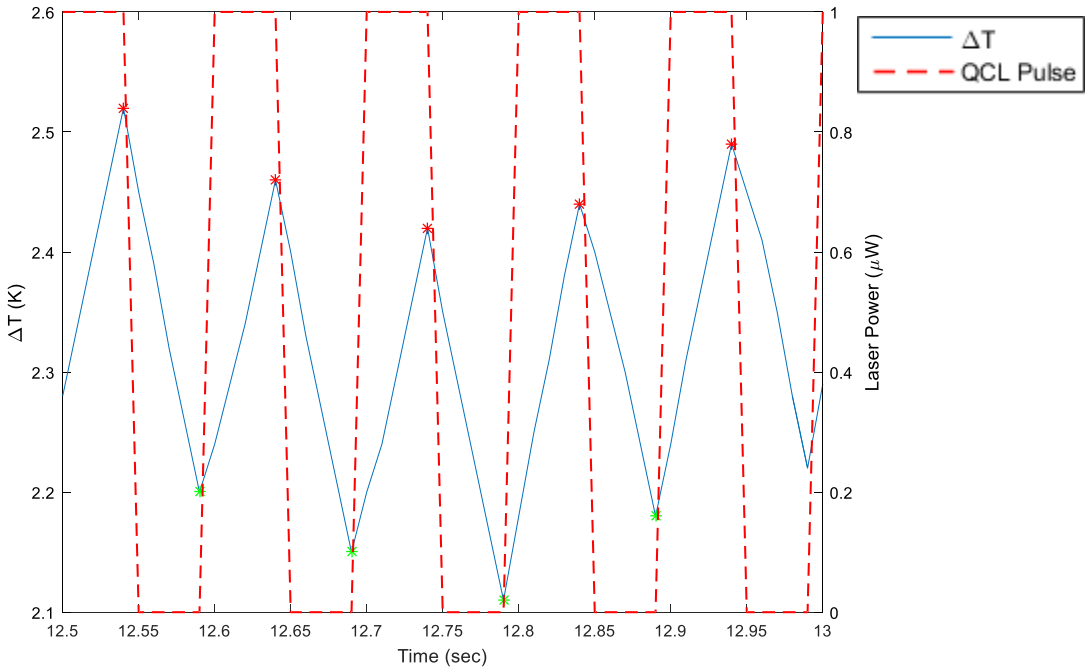

Figure 23. Time Domain Response for One Sensor Under Illumination of 1 μW Incident Laser Power Gated at 10 Hz.

Figure 23 also shows what happens when the sensor is operated at a frequency much higher than the thermal time constant allows. Not enough time is provided for the sensor to cool down via thermal heat conductance. The net effect is that the minimum temperature never returns back to ambient room temperature, and this results in a steady-state minimum temperature which is 2.1 K above room temperature.

The normalized frequency response is shown in Figure 24. Of note, the 3dB bandwidth is 0.65 Hz resulting in a thermal time constant for the sensor model of:

$$\tau = \frac{1}{2\pi f_{3dB}} = \frac{1}{2\pi(0.65Hz)} = 0.245\text{sec} \tag{41}$$

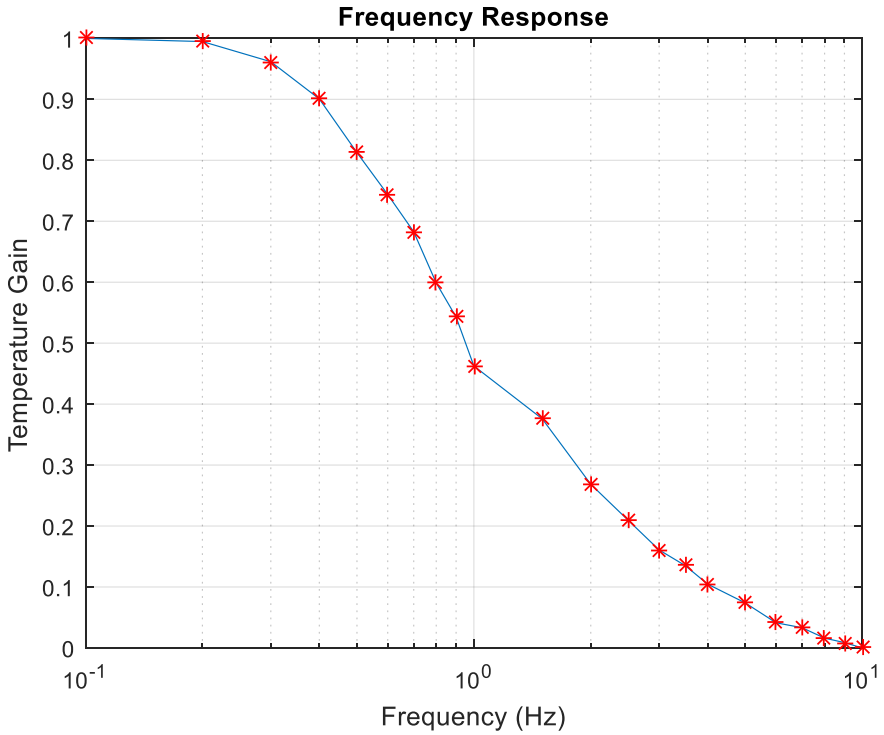

Figure 24. Normalized Frequency Response for One Sensor Under Illumination with 1 µW Incident Laser Power where the Gating Frequency is the Independent Variable.

THIS PAGE INTENTIONALLY LEFT BLANK

IV. EXPERIMENTAL REALIZATION AND RESULTS

A. CHARACTERIZATION OF THE THZ TO IR CONVERTER SENSOR

In order to characterize the sensor, the THz FPA had to be positioned so as to focus as much laser power as possible on to a single detector. Fortunately, even though the silicon nitride detector of a microbolometer camera is optimized for infrared it has just enough sensitivity in the THz range to detect it. The only problem is that the anti-reflective coating on the Germanium lens of the microbolometer camera makes it opaque to THz and hence had to be removed as shown in Figure 25.

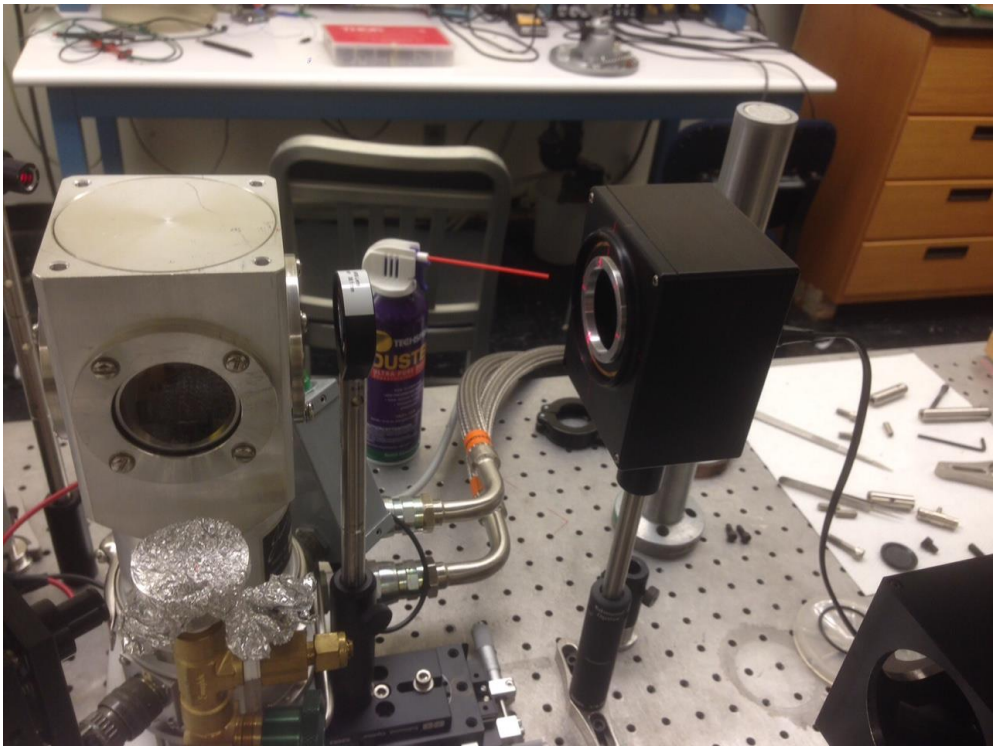

Figure 25. Microbolometer Camera with Germanium Lens Removed to Detect THz from QCL to Find Focal Point.

The resulting image of the laser's beam as captured by the microbolometer camera is shown in Figure 26.

Figure 26. QCL Beam Captured by Microbolometer Camera.

Once the focal point was found the exact position was marked by shining two displaced lasers at the microbolometer array and adjusting their position until they intersected at the center as shown in Figure 27.

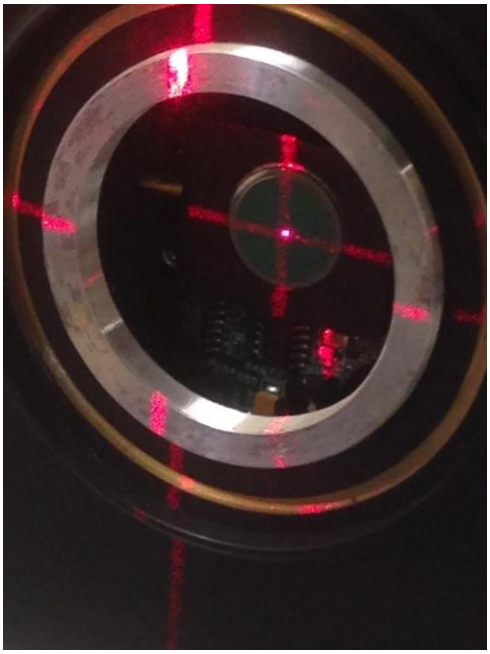

Figure 27. Marking Position of QCL Focal Point by Using Two Displaced Lasers and Adjusting their Position until they Intersected at the Center of the Microbolometer Array.

The THz FPA is placed in a vacuum chamber and positioned at the focal point of the QCL and Si lens. Then a FLIR A20 infrared camera was placed behind the FPA to detect the change in temperature of the sensor due to absorption of THz energy from the QCL. The setup is shown in Figure 28.

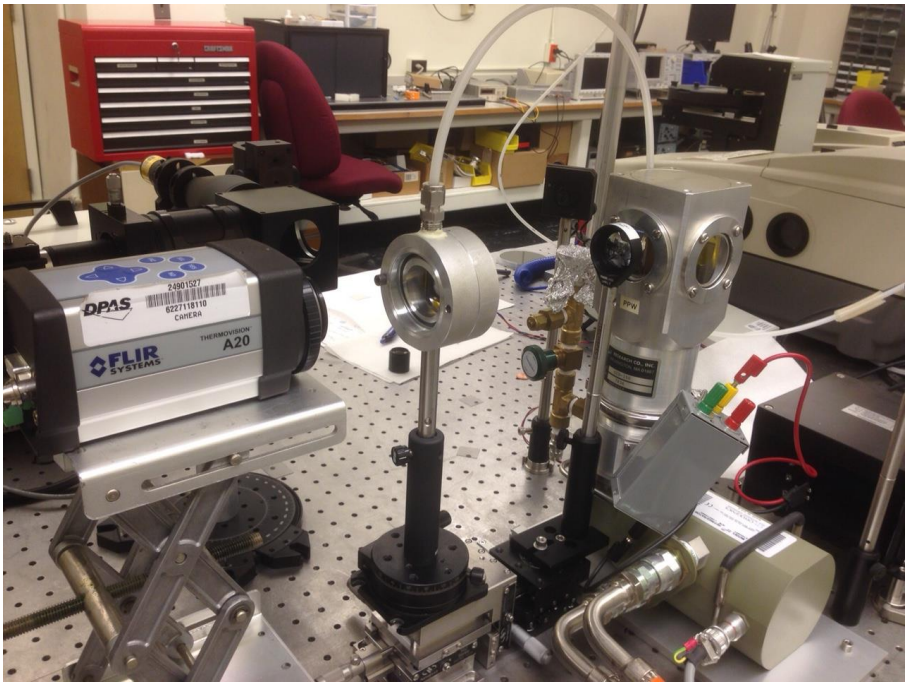

Figure 28. Experimental Setup Used to Measure the Change in Temperature of the Detector Illuminated by a QCL.

Figure 29 shows the resulting infrared images of the backside of the detector before and after it has been illuminated with the quantum cascade laser.

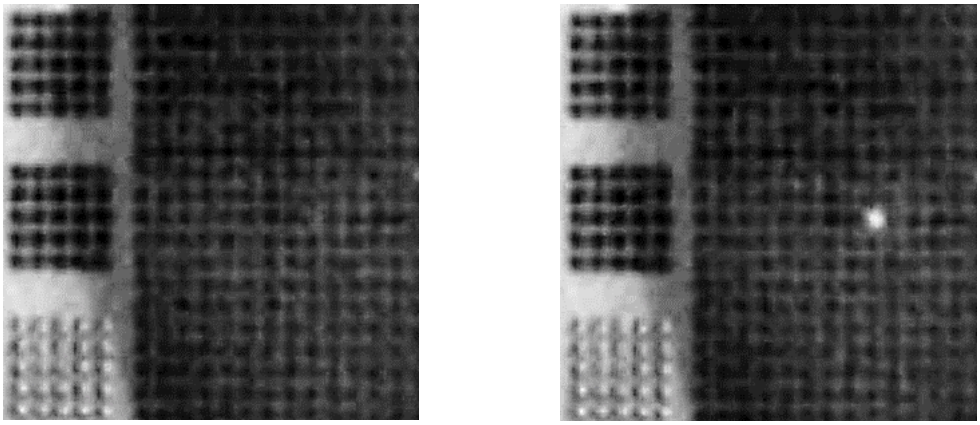

Figure 29. Infrared Image of FPA with QCL Off (Left). FPA with QCL On (Right).

To determine the frequency response of the sensor, the laser was set to its maximum recommended power, which gives 1 μW of power incident on a single pixel. The laser was then gated from 0.1 Hz to 10 Hz while the microbolometer camera captured and recorded the temperature of the sensor through the use of National IR Software. The results were analyzed and plotted using MATLAB®. The time domain responses are shown in Figures 30 and 31.

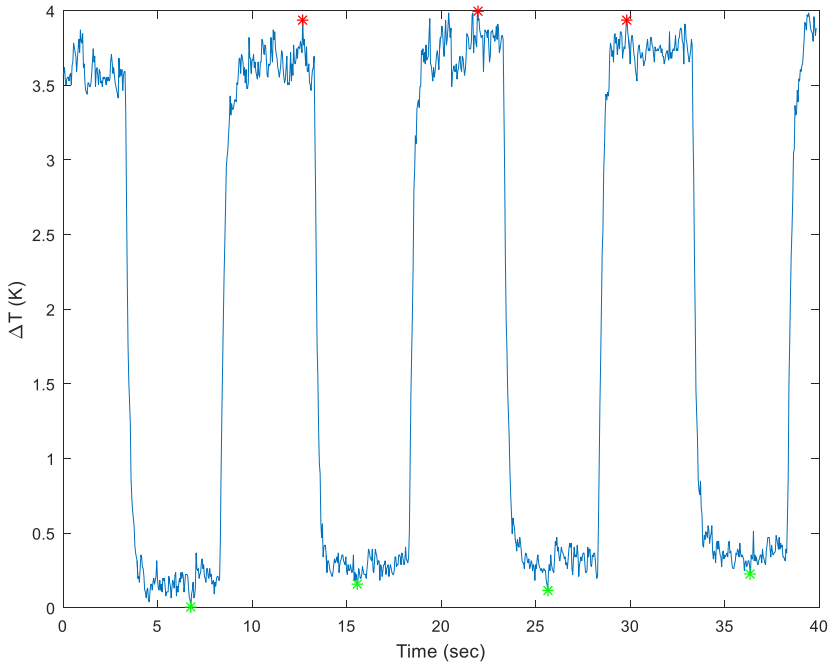

Figure 30. Time Domain Response of the Sensor Recorded Using an IR Camera when Illuminated Under 1 µW Laser Gated at 0.1 HZ.

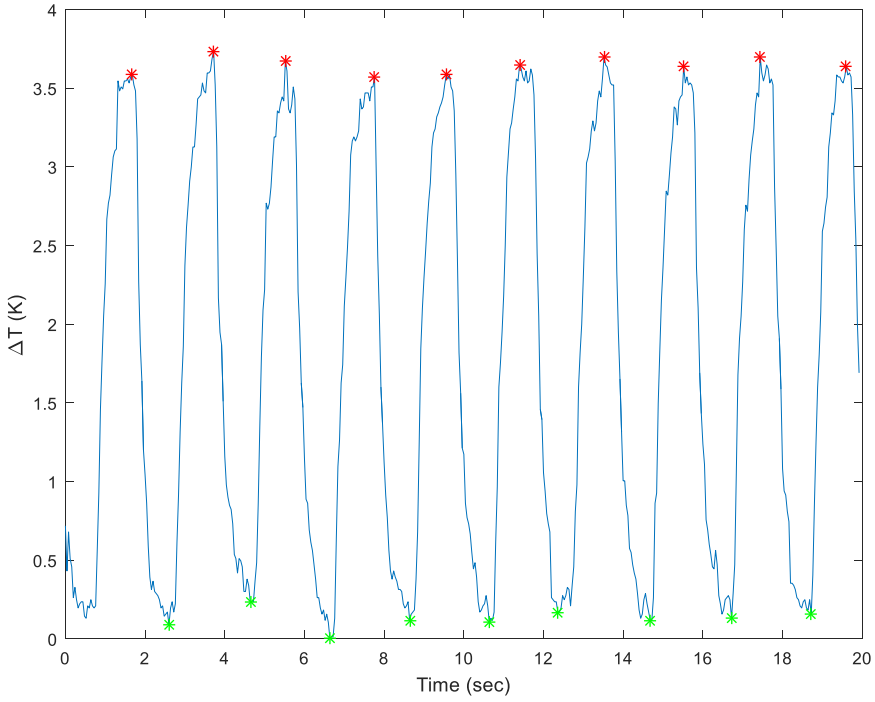

Figure 31. Time Domain Response of the Sensor Recorded Using an IR Camera when Illuminated Under 1 µW Laser Gated at 0.5 HZ.

The difference between the average maxima (highlighted in red) and minima (highlighted in green) was used to determine the average ΔT. Additionally, a filtering algorithm was implemented that evaluated the rate of change of the temperature at any given point and compared it with neighboring points so as not to factor in the average any abrupt changes due to the presence of noise.

The normalized frequency response is shown in Figure 32. The 3dB bandwidth is 0.94 Hz resulting in a time constant for the sensor model of:

$$\tau = \frac{1}{2\pi f_0} = \frac{1}{2\pi(0.94Hz)} = 0.169\,\text{sec} \tag{42}$$

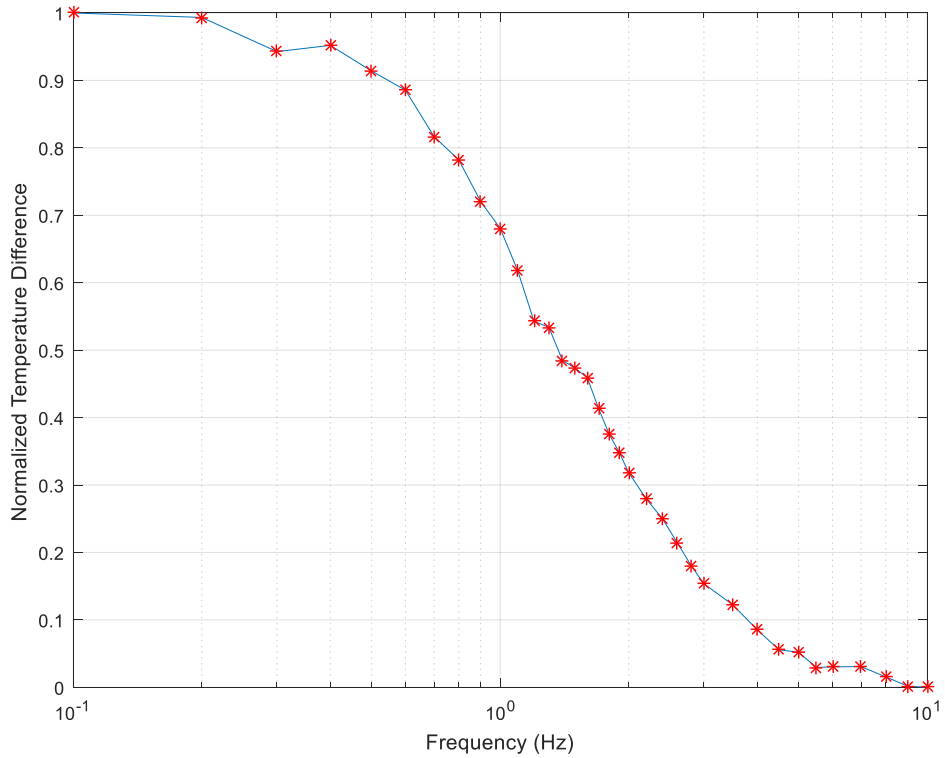

Figure 32. Normalized Frequency Response for 3.8 THz-to-IR Detector Under Illumination of 1 μW Incident Laser Power where the Gating Frequency is the Independent Variable.

To determine the power sensitivity of the detector, the laser was set at a nominal gate frequency of 0.5 Hz and the incident laser power at the detector was varied from 0.025 μW to 1.0 μW. As shown in Figure 33, for 0.5 μW and 1 μW of incident power gated at 0.5 Hz, ΔT increased with an increase in incident laser power.

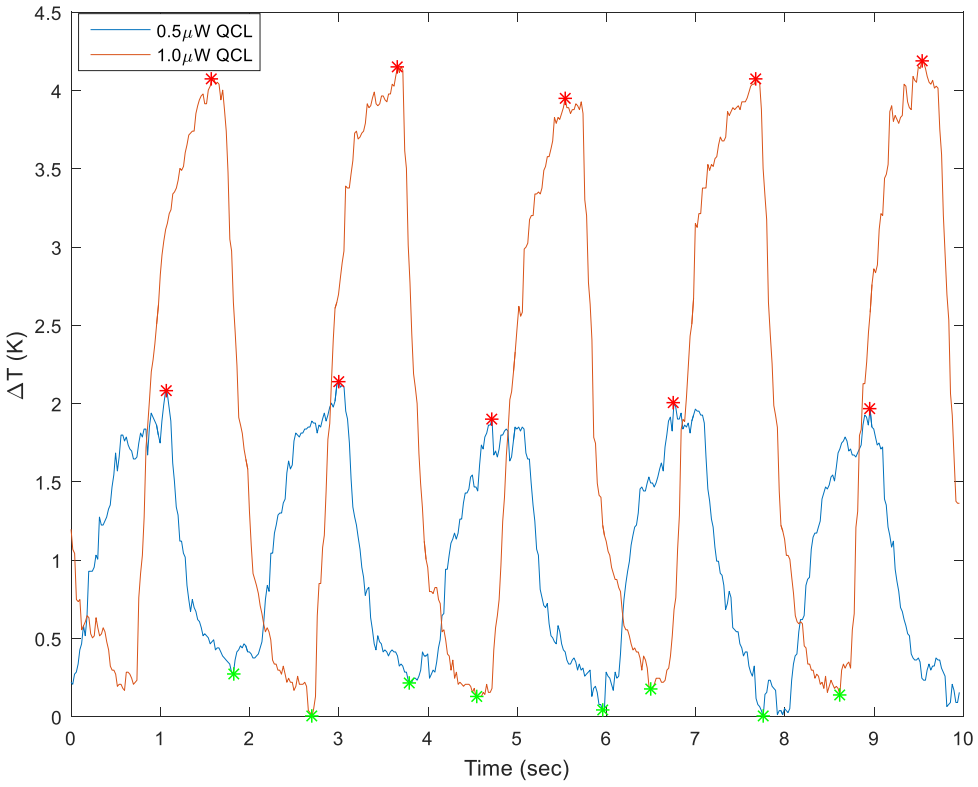

Figure 33. Comparison Between 3.8 Thz to IR Detector Time Domain Response when Illuminated Under a 0.5 μW and 1 μW Laser Gated at 0.5 HZ.

The temporal response displayed a linear relationship with incident THz power as depicted in Figure 34 and agrees well with that of the simulated using COMSOL® model. The thermal sensitivity was found to be 3.6 $K/\mu W$ compared to 3.0 $K/\mu W$ in the COMSOL® model. The difference is probably due to a slightly higher laser power incident on the sensor than was used in the simulation. As the laser is operated for any period of time it warms up and results in a reduction in

power which would lead to underestimating maximum power available when it is cold. Another possibility lies with the FLIR camera software and the way the algorithm assigns a temperature value to a detected IR signature. For instance, user defined emissivity values will result in a wide range of displayed temperature values.

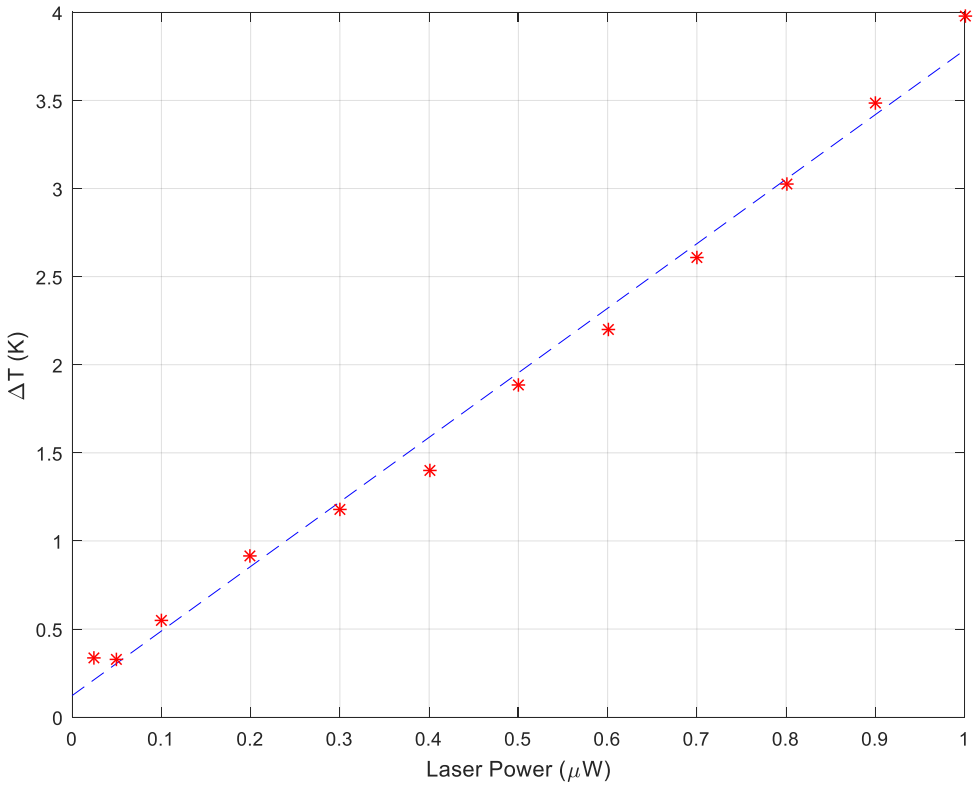

Figure 34. Measured Temperature Change as a Function of Laser Power on the Detector.

B. CHARACTERIZATION OF OPTICAL READOUT

In order to characterize the optical readout of FPA, the setup in Figure 35 was utilized.

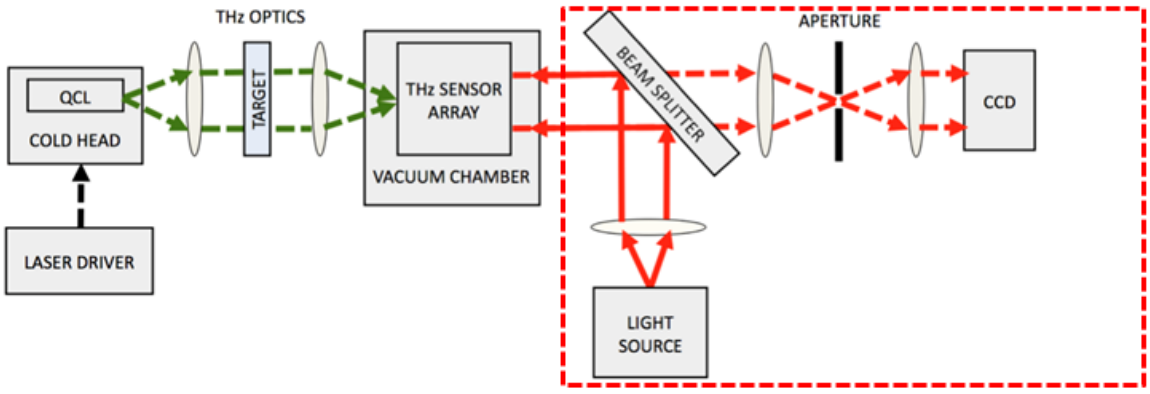

Figure 35. QCL and Optical Readout Schematic.

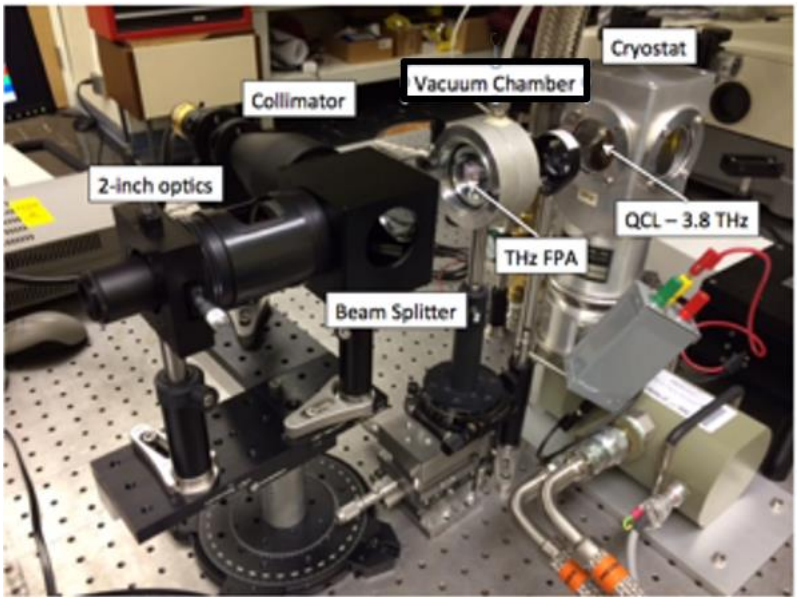

Figure 36. Experimental Optical Readout Setup.

The output from the CCD camera was analyzed using a differential LabView routine in order to enhance the image. First a background image with

the QCL turned off was obtained, Figure 37. This image was then subtracted from subsequent images with the QCL turned on to only image those pixels that experienced a change in angular displacement due to THz radiation. This resulted in a change in light intensity as shown in Figure 38.

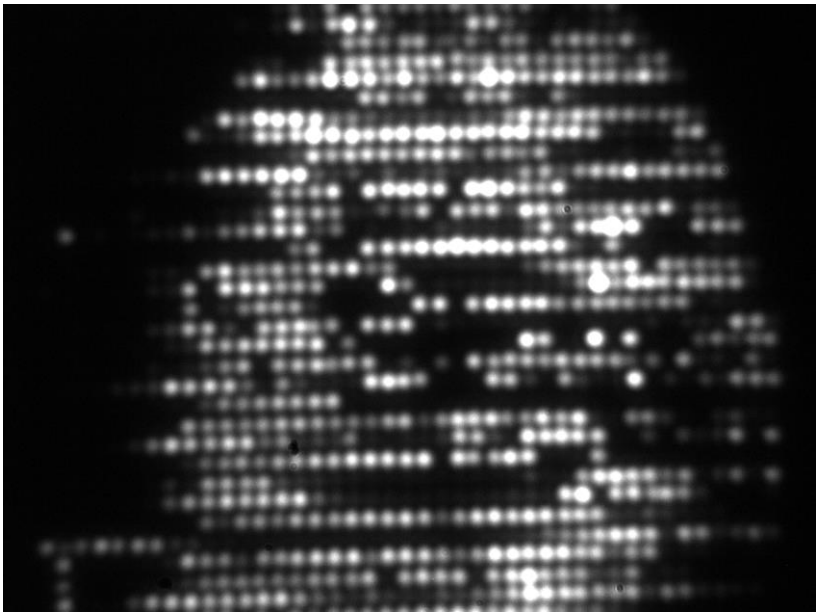

Figure 37. Background Image with QCL Off.

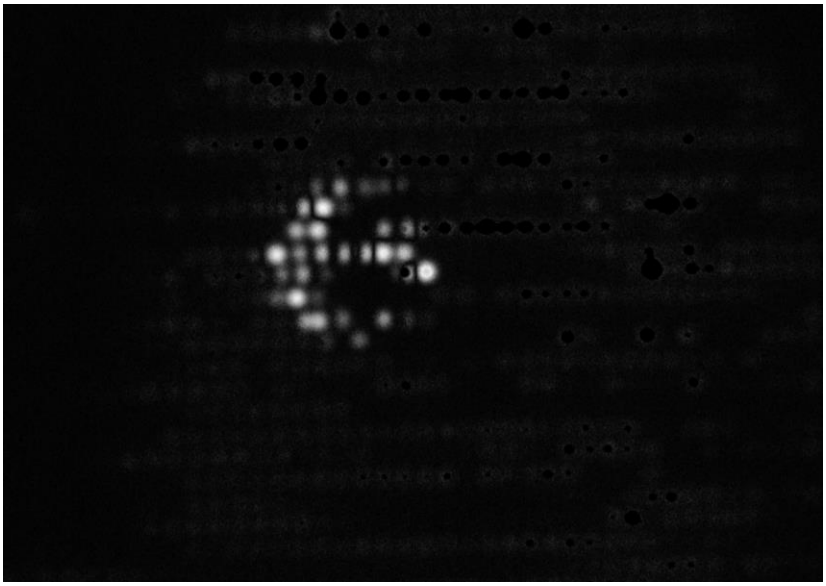

Figure 38. Differential Image with QCL On.

The output of the QCL was gated from 0.1 Hz to 10 Hz and the intensity level at one pixel was recorded in the time domain. The results were analyzed in MATLAB and are shown in Figures 39 and 40.

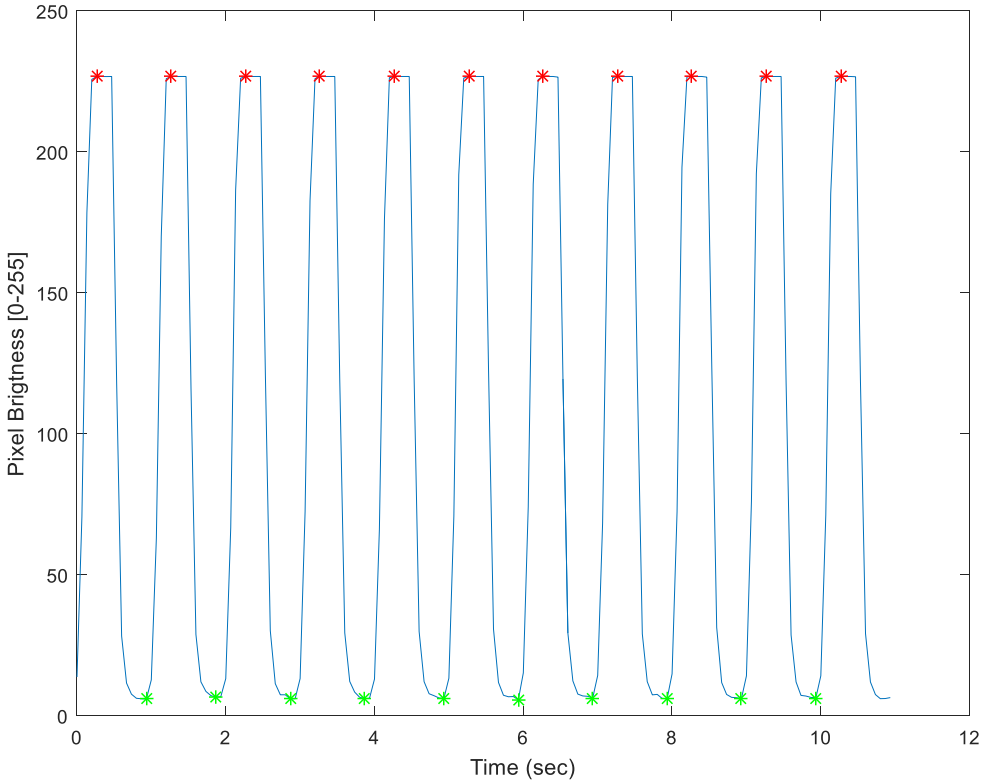

Figure 39. Pixel Brightness for 1 Hz Gated Laser Power.

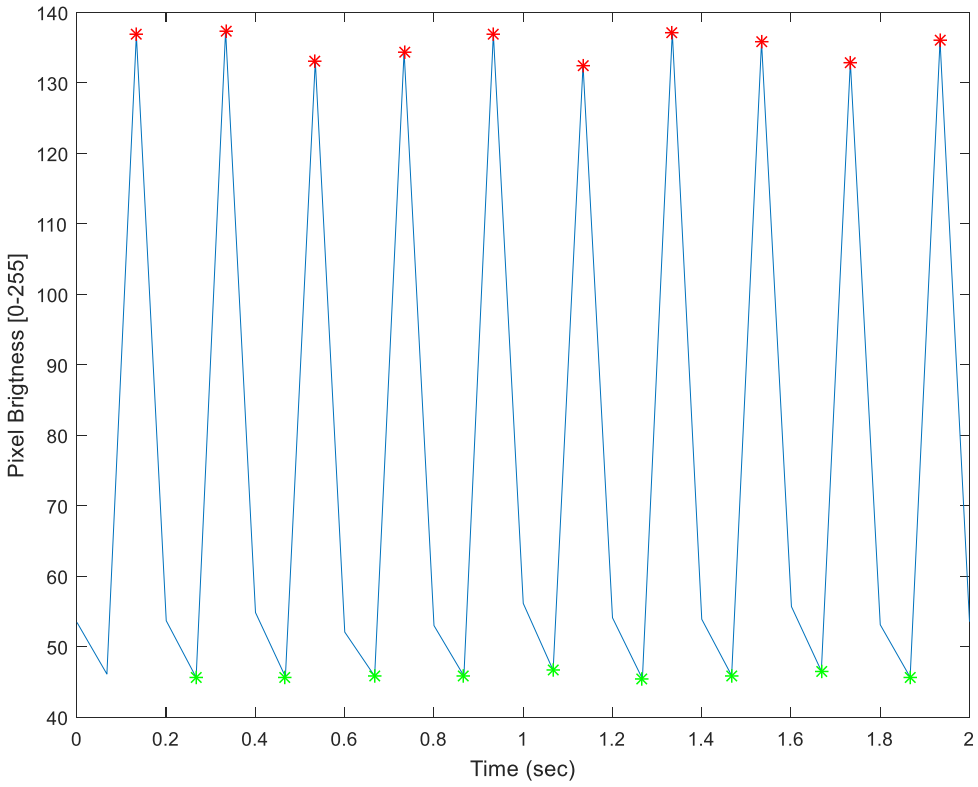

Figure 40. Pixel Brightness for 5 Hz Gated Laser Power.

The frequency response is shown in Figure 41. The 3dB bandwidth is at 3.4 Hz resulting in a time constant for the optical readout system of:

$$\tau = \frac{1}{2\pi f_0} = \frac{1}{2\pi(3.4Hz)} = 0.047\,\text{sec} \tag{43}$$

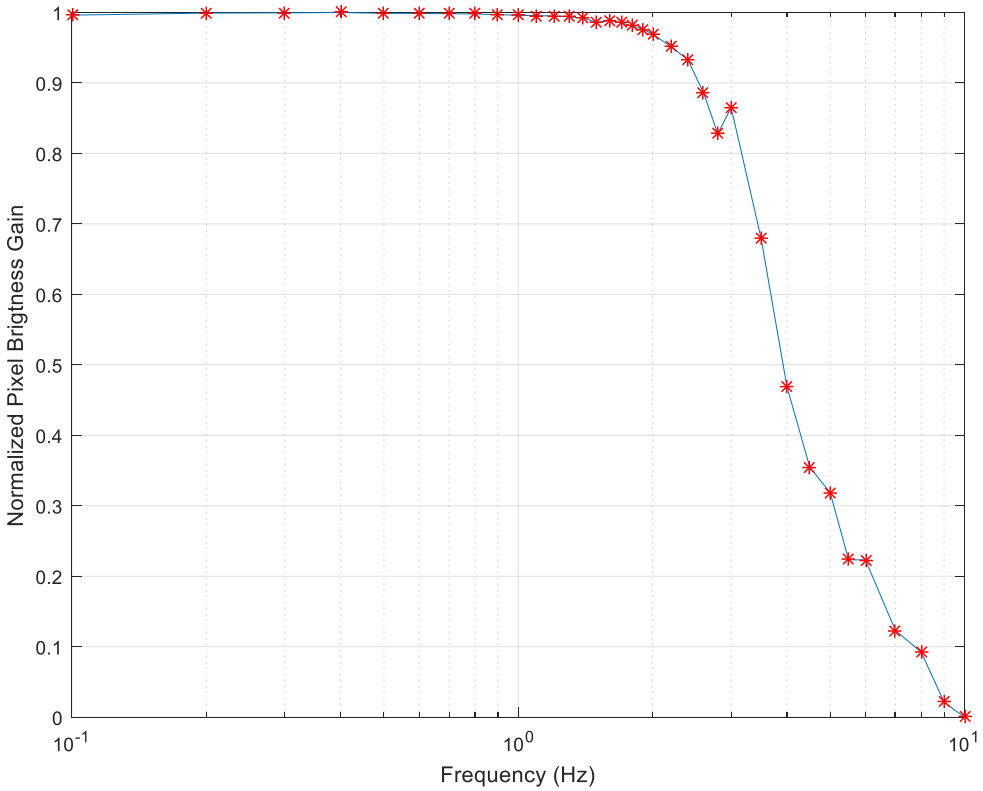

Figure 41. Normalized Frequency Response Acquired Using the Optical Readout.

C. INTERPRETATION OF FINDINGS

For the THz-to-IR converter it was found that frequency response was 0.65 Hz compared to 2.4 Hz for sensor with optical readout. The difference is mainly due to higher thermal isolation of the sensor used in THz to IR conversion. Such a low frequency response limits its usability to still images. In order to have the ability to capture video the speed of operation inversely related to the time constant ($\tau = \frac{C}{G}$) would have to be increased by either reducing the heat capacitance, C, or increasing the thermal conductance, G. As previously discussed an increased in thermal conductance would reduce the sensitivity, $\Re = \frac{\eta}{G}\frac{\Delta\theta}{\Delta T}$, resulting in a loss of quality in a video application.

THIS PAGE INTENTIONALLY LEFT BLANK

V. CONCLUSION

While the terahertz spectrum continues to remain a relatively untapped portion of the electromagnetic spectrum, the ability to penetrate many materials presents an exciting opportunity for imaging applications.

It was demonstrated that by mounting a metamaterial absorber sensitive to THz waves on bi-material legs and incorporating a highly reflective aluminum layer on the backside each sensor would behave like a movable mirror that could be probed with visible light. An optical readout was implemented in order to analyze and recreate the target image.

The quality and magnification of the optical readout was controlled by careful selection of its optical components (wavelength, lens, aperture, CCD camera).

In addition a THz-to-IR converter was characterize both in frequency and power responsiveness in order to determine compatibility with an IR camera. These results closely matched those found through computer modeling.

Future work will focus on the fabrication of a THz FPA with more closely packed sensors which will allow a higher resolution. Also additional investigation into the optimal aperture size is necessary given the angular deflection of the sensor.

THIS PAGE INTENTIONALLY LEFT BLANK

APPENDIX A. MATLAB CODE FOR THZ TO IR EXPERIMENTAL RESULTS

```
%THZ_IR
%4 Feb 2016

clc, clear all,close all

startRow = 2;
endRow = inf;
deltaT = [];
timeRel = [];
freq = [0.1 0.2 0.3 0.4 0.5 0.6 0.7 0.8 0.9 1.0 1.1 1.2 1.3 1.4 1.5
1.6...
        1.7 1.8 1.9 2.0 2.2 2.4 2.6 2.8 3.0 3.5 4.0 4.5 5.0 5.5 6.0
7.0...
        8.0 9.0 10.0];

for i = 1:length(freq)
    fileName = sprintf('%1gHz.txt',freq(i));
    [frame,time,Cursor2,Cursor1] =
importfile(fileName,startRow,endRow);
    if isempty(frame)
        continue
    end

    if freq(i) < 0.5
        index = 997;
    elseif freq(i) < 1
        index = 499;
    else
        index = 247;
    end
    time = time(1:index,:);
    Cursor2 = Cursor2(1:index,:);
    Cursor2 = Cursor2 - min(Cursor2);
    for j = 1:length(time)
        timeRel(j) = etime(datevec(time(j)),datevec(time(1)));
    end
    timeRel = timeRel(:,1:index);

    [imax2, peakMax] = peakfinder(Cursor2,(max(Cursor2)-
min(Cursor2))/3,[],1, false);
    [imin2, peakMin] = peakfinder(Cursor2,(max(Cursor2)-
min(Cursor2))/3,[],-1, false);
    maxMean = mean(peakMax);
    minMean = mean(peakMin);

    deltaT(i) = maxMean-minMean;

    if freq(i) == 0.1 || freq(i) == 0.5 || freq(i) == 1 || freq(i) == 2
|| freq(i) == 5 || freq(i) == 10
```

```
        figure
        plot(timeRel, Cursor2)
        hold on

plot(timeRel(imax2),Cursor2(imax2),'r*',timeRel(imin2),Cursor2(imin2),'
g*')
        xlabel('Time (sec)')
        ylabel('\DeltaT (K)')
        title([num2str(freq(i)), ' Hz Laser Frequency'])
        hold off
        fprintf('\nFreq: %2.1f Hz   DeltaT: %2.2f K\n', freq(i),
deltaT(i))
    end
end

deltaTmax = max(deltaT);
deltaTmin = min(deltaT);
normDeltaT = (deltaT-deltaTmin)/(deltaTmax-deltaTmin);

figure
semilogx(freq, normDeltaT)
hold on
semilogx(freq, normDeltaT, 'r*')
hold off
ax = gca;
ax.YTick = 0:0.1:1.0;
ax.FontSize = 12;
xlabel('Frequency (Hz)', 'FontSize', 16)
ylabel('Normalized Temperature Difference', 'FontSize', 16)
%title('Frequency Response')
grid on


freq = freq';
normDeltaT = normDeltaT';
dlmwrite('freq_resp.csv',[freq normDeltaT],'delimiter',',')

deltaT = [];
timeRel = [];
freq = [0.25 0.50 1 2 3 4 5 6 7 8 9 10]; %laser power in kHz
power = freq/10; %power in uW
for i = 1:length(freq)
    fileName = sprintf('%1gkHz_Power.txt',freq(i));
    [frame,time,Cursor2,Cursor1] =
importfile(fileName,startRow,endRow);
    if isempty(frame)
        continue
    end

        index = 499;
    time = time(1:index,:);
    Cursor2 = Cursor2(1:index,:);
    Cursor2 = Cursor2 - min(Cursor2);
    for j = 1:length(time)
```

```
        timeRel(j) = etime(datevec(time(j)),datevec(time(1)));
    end
    timeRel = timeRel(:,1:index);

    [imax2, peakMax] = peakfinder(Cursor2,(max(Cursor2)-
min(Cursor2))/3,[],1, false);
    [imin2, peakMin] = peakfinder(Cursor2,(max(Cursor2)-
min(Cursor2))/2,[],-1, false);
    maxMean = mean(peakMax);
    minMean = mean(peakMin);

    deltaT(i) = maxMean-minMean;

    if freq(i) == 5
        timeRel_5 = timeRel;
        Cursor2_5 = Cursor2;
        imax2_5 = imax2;
        imin2_5 = imin2;
    end
    if freq(i) == 10
        timeRel_10 = timeRel;
        Cursor2_10 = Cursor2;
        imax2_10 = imax2;
        imin2_10 = imin2;
    end
%     if freq(i) == 0.25 || freq(i) == 1 || freq(i) == 5 || freq(i) ==
10
%         figure
%         plot(timeRel, Cursor2)
%         hold on
%
plot(timeRel(imax2),Cursor2(imax2),'r*',timeRel(imin2),Cursor2(imin2),'
g*')
%         xlabel('Time (sec)')
%         ylabel('\DeltaT (K)')
%         title([num2str(power(i)), ' uW Laser Power'])
%         hold off
%         fprintf('\nPower: %1.2f uW   DeltaT: %2.2f K\n', power(i),
deltaT(i))
%     end
end

deltaTmax = max(deltaT);
deltaTmin = min(deltaT);
normDeltaT = (deltaT-deltaTmin)/(deltaTmax-deltaTmin);

figure
hold on
%p = polyfit(power,normDeltaT,1);
p = polyfit(power,deltaT,1);
x_values = [0 power];
f = polyval(p,x_values);
plot(x_values,f,'--b')
%plot(power, normDeltaT,'r*')
```

```
plot(power, deltaT,'r*')
hold off
ax = gca;
ax.YTick = 0:0.5:4.0;
ax.FontSize = 12;
xlabel('Laser Power (\muW)', 'FontSize', 16)
ylabel('\DeltaT (K)', 'FontSize', 16)
%title('Power Response')
grid on
box on

power = power';
%normDeltaT = normDeltaT';
%dlmwrite('power_resp.csv',[power normDeltaT],'delimiter',',')

figure
plot(timeRel_5, Cursor2_5, timeRel_10, Cursor2_10)
hold on
plot(timeRel_5(imax2_5),Cursor2_5(imax2_5),'r*',timeRel_5(imin2_5),Curs
or2_5(imin2_5),'g*')
plot(timeRel_10(imax2_10),Cursor2_10(imax2_10),'r*',timeRel_10(imin2_10
),Cursor2_10(imin2_10),'g*')
xlabel('Time (sec)')
ylabel('\DeltaT (K)')
title([num2str(power(i)), ' uW Laser Power'])
hold off
```

APPENDIX B. MATLAB CODE FOR THZ TO IR SIMULATION RESULTS

```
%Comsol_Data
%31 Mar 2016

clc, clear all,close all

startRow = 1;
endRow = inf;
deltaT = [];
freq = [];
fileName = 'THz2IR_run1.csv';
[freq_all,time_all,temp_all] = importfile(fileName,startRow,endRow);
temp_all = temp_all - 293.15;

i = 1;
while i <= length(freq_all)
    time = [];
    temp = [];
    freq(end+1) = freq_all(i);

    while i <= length(freq_all) && freq(end) == freq_all(i)
        time(end+1) = time_all(i);
        temp(end+1) = temp_all(i);
        i = i+1;
    end

    [imax2, peakMax] = peakfinder(temp,(max(temp)-min(temp))/3,[],1,
false);
    [imin2, peakMin] = peakfinder(temp,(max(temp)-min(temp))/3,[],-1,
false);
    maxMean = mean(peakMax);
    minMean = mean(peakMin);

    deltaT(end+1) = maxMean-minMean;

    figure
    plot(time, temp)
    hold on
    plot(time(imax2),temp(imax2),'r*',time(imin2),temp(imin2),'g*')
    xlabel('Time (sec)')
    ylabel('\DeltaT (K)')
    title([num2str(freq(end)), ' Hz Laser Frequency'])
    hold off
    fprintf('\nFreq: %2.1f Hz   DeltaT: %2.2f \n', freq(end),
deltaT(end))
end

fileName = 'QCL_run2.csv';
[~,~,power_all] = importfile(fileName,startRow,endRow);
```

```
power_all = power_all/0.99676;
fileName = 'THz2IR_run2.csv';
[freq_all,time_all,temp_all] = importfile(fileName,startRow,endRow);
temp_all = temp_all - 293.15;

i = 1;
while i <= length(freq_all)
    time = [];
    temp = [];
    power = [];
    freq(end+1) = freq_all(i);

    while i <= length(freq_all) && freq(end) == freq_all(i)
        time(end+1) = time_all(i);
        temp(end+1) = temp_all(i);
        power(end+1) = power_all(i);
        i = i+1;
    end

    [imax2, peakMax] = peakfinder(temp,(max(temp)-min(temp))/3,[],1,
false);
    [imin2, peakMin] = peakfinder(temp,(max(temp)-min(temp))/3,[],-1,
false);
    maxMean = mean(peakMax);
    minMean = mean(peakMin);

    deltaT(end+1) = maxMean-minMean;

        figure
    [ax,p1,p2] = plotyy(time, temp, time, power);
    hold on
    plot(time(imax2),temp(imax2),'r*',time(imin2),temp(imin2),'g*')
    set(p2,'LineStyle','--', 'LineWidth', 1.2, 'Color', 'red')
    ax(1).YColor = 'black'; ax(2).YColor = 'black';
    xlabel('Time (sec)')
    ylabel(ax(1),'\DeltaT (K)')
    ylabel(ax(2),'Laser Power (\muW)')
    title([num2str(freq(end)), ' Hz Laser Frequency'])
    legend([p1, p2], '\DeltaT','QCL Pulse','Location','northoutside')
    hold off

    fprintf('\nFreq: %2.1f Hz   DeltaT: %2.2f \n', freq(end),
deltaT(end))
end

fileName = 'QCL_run3.csv';
[~,~,power_all] = importfile(fileName,startRow,endRow);
power_all = power_all/0.0000011396;
fileName = 'THz2IR_run3.csv';
[freq_all,time_all,temp_all] = importfile(fileName,startRow,endRow);
temp_all = temp_all - 293.15;

i = 1;
while i <= length(freq_all)
```

```
    time = [];
    temp = [];
    power = [];
    freq(end+1) = freq_all(i);

    while i <= length(freq_all) && freq(end) == freq_all(i)
        if time_all(i) >= 11
            time(end+1) = time_all(i);
            temp(end+1) = temp_all(i);
            power(end+1) = power_all(i);
        end
        i = i+1;
    end

    [imax2, peakMax] = peakfinder(temp,(max(temp)-min(temp))/3,[],1,
false);
    [imin2, peakMin] = peakfinder(temp,(max(temp)-min(temp))/3,[],-1,
false);
    maxMean = mean(peakMax);
    minMean = mean(peakMin);

    deltaT(end+1) = maxMean-minMean;

    figure
    [ax,p1,p2] = plotyy(time, temp, time, power);
    hold on
    plot(time(imax2),temp(imax2),'r*',time(imin2),temp(imin2),'g*')
    set(p2,'LineStyle','--', 'LineWidth', 1.2, 'Color', 'red')
    ax(1).YColor = 'black'; ax(2).YColor = 'black';
    xlabel('Time (sec)')
    ylabel(ax(1),'\DeltaT (K)')
    ylabel(ax(2),'Laser Power (\muW)')
    title([num2str(freq(end)), ' Hz Laser Frequency'])
    legend([p1, p2], '\DeltaT','QCL Pulse','Location','northoutside')
    hold off

    fprintf('\nFreq: %2.1f Hz   DeltaT: %2.2f \n', freq(end),
deltaT(end))
end

deltaTmax = max(deltaT);
deltaTmin = min(deltaT);
normDeltaT = (deltaT-deltaTmin)/(deltaTmax-deltaTmin);

figure
semilogx(freq, normDeltaT)
hold on
semilogx(freq, normDeltaT, 'r*')
hold off
xlabel('Frequency (Hz)')
ylabel('Normalized Temperature Difference')
box on
grid on
```

```
freq = freq';
normDeltaT = normDeltaT';
%dlmwrite('freq_resp.csv',[freq normDeltaPix],'delimiter',',')


fileName = 'powerresp.csv';
[power,temp] = importfile(fileName,startRow,endRow);

deltaT = temp-293.15;

deltaTmax = max(deltaT);
deltaTmin = min(deltaT);
normDeltaT = (deltaT-deltaTmin)/(deltaTmax-deltaTmin);

figure
hold on
%p = polyfit(power,normDeltaT,1);
p = polyfit(power,deltaT,1);
x_values = [0; power];
f = polyval(p,x_values);
plot(x_values,f,'--b')
%plot(power, normDeltaT,'r*')
plot(power, deltaT,'r*')
hold off
xlabel('Laser Power (\muW)')
ylabel('\DeltaT (K)')
grid on
box on

fileName = 'temprise_01uW.csv';
[time,temp] = importfile(fileName,startRow,endRow);

deltaT = temp-293.15;

t = 0:0.01:3;
tau2 = -time./log(-(deltaT/0.3 - 1));
tau2(1) = []; tau2(15:end) = [];
tau = mean(tau2);

y = 0.3*(1 - exp(-t/tau));
figure
hold on
plot(t,y,'-b')
plot(time,deltaT,'r*')

fileName = 'temprise_1uW.csv';
[time,temp] = importfile(fileName,startRow,endRow);

deltaT = temp-293.15;

t = 0:0.01:3;
tau2 = -time./log(-(deltaT/3 - 1));
tau2(1) = []; tau2(end) = [];
```

```
tau = mean(tau2);

y = 3*(1 - exp(-t/tau));
plot(t,y,'-b')
plot(time,deltaT,'r*')
hold off
xlabel('Time (s)')
ylabel('\DeltaT (K)')
box on

BW = 1/(2*pi*tau);
```

THIS PAGE INTENTIONALLY LEFT BLANK

APPENDIX C. MATLAB CODE FOR LENS SETUP

```
%Lens Characterization

clc, clear all, close all

n1 = 1.6725; %index of refraction of E-BAF11 for 520nm (green led)
n2 = 1.7975; %index of refraction of N-SF11 for 520nm (green led)

R1 = 50.8;
R2 = -41.7;
R3 = -247.7;

t1 = 20;
t2 = 3;

M1 = [1 0;1/R3*(n2-1) n2]*[1 3;0 1]*[1 0;1/R2*(n1/n2-1) n1/n2]*[1 20;0
1]*[1 0;1/R1*(1/n1-1) 1/n1];
A = M1(1,1); B = M1(1,2); C = M1(2,1); D = M1(2,2);

f1 = 1/C; f2 = -1/C;
r = 1/C*(D-1); s = (1-A)/C;
L1_F1 = f1+r;
L1_F2 = f2+s;


n1 = 1.5168; %index of refraction of N-BK7 for 520nm (green led)
R = 24.397;
t1 = 10.132;

M2 = [1 0;1/-R*(n1-1) n1]*[1 10.132;0 1]*[1 0;1/R*(1/n1-1) 1/n1];
A = M2(1,1); B = M2(1,2); C = M2(2,1); D = M2(2,2);

f1 = 1/C; f2 = -1/C;
r = 1/C*(D-1); s = (1-A)/C;
L2_F1 = f1+r;
L2_F2 = f2+s;


D1 = 50.8;
D2 = 25.4;
D3 = 20.3;
D4 = 4.8;

% Y1 = [1 L1_F2;0 1]*M1*[D1/2;0];
%
% fun = @(x1)-D2*1/2 - [1 0]*[1 x1;0 1]*Y1;
% [x1,fval] = fsolve(fun,10);
%
% Y2 = M2*[1 x1;0 1]*Y1;
% fun = @(x3)D4/2 - [1 0]*[1 x3;0 1]*Y2;
```

```
% [x3,fval] = fsolve(fun,10);
%
% x2 = x3 - (20.6+1.7);
%
% Y3 = [1 x2;0 1]*Y2
%
% X1 = x1 - 10.6 + 0.5 + 3.15
% X2 = x2 + 3 + 0.5
% total = X1 + X2 + 6 + 2*2.14

% Y1 = [1 L1_F2;0 1]*M1*[11;0];
%
% fun = @(x1)[0 1]*M2*[1 5;0 1]*M2*[1 x1;0 1]*Y1;
% [x1,fval] = fsolve(fun,10)

Y1 = [1 L1_F2;0 1]*M1*[11;0];

fun = @(x1)[0 1]*M2*[1 x1;0 1]*Y1;
[x1,fval] = fsolve(fun,10)

L1_L2 = x1 + L1_F2; %Distance required between lens 1 and 2 for a
collimated beam

theta = 0.0109; %rad
s = 2000; %mm (no less than 118mm, currently setup at 180mm)
Y1 = [1 L1_F2;0 1]*M1*[s*theta;theta];
M3 = [1 0;1/2 1];

% theta = -.1:.0001:.1;
% y = 0;
% for i = 1:length(theta)
%     y(i) = 0.150 - [1 0]*[1 L1_F2;0 1]*M1*[1 s;0
1]*([0;theta(i)]+M3*[200e-3/2;0]);
% end
% plot(theta*180/pi,y)

fun = @(theta)0.150 - [1 0]*[1 L1_F2;0 1]*M1*[1 s;0 1]*([0;theta]+M3*[-
200e-3/2;0]);
[theta,fval] = fsolve(fun,0.01);

theta_deg = theta*180/pi
```

APPENDIX D. ACHROMAT DOUBLET LENS SPECIFICATIONS

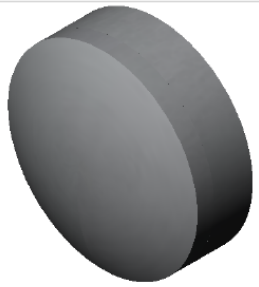

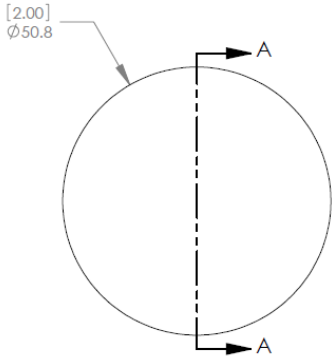

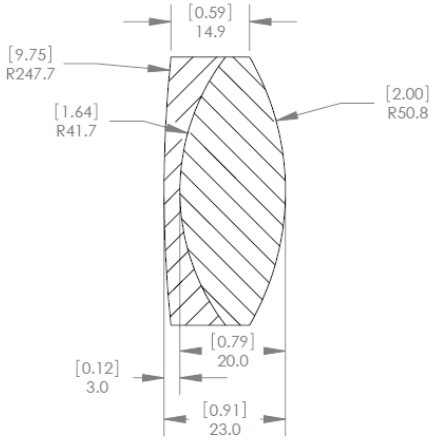

SECTION A-A

NOTES/SPECIFICATIONS:

DESIGN WAVELENGTH: 486.1nm, 587.6nm, & 656.3nm
FOCAL LENGTH: 75.0mm ± 1%
BACK FOCAL LENGTH (REF): 61.8mm
CLEAR APERTURE: >90%
SURFACE QUALITY: 40-20 SCRATCH-DIG
CENTRATION: <3 arcmin
DIAMETER TOLERANCE: +0.0/-0.1mm
THICKNESS TOLERANCE: ± 0.15mm
COATING: BBAR Ravg <0.5% FROM 400nm-700nm
0° AOI, ON BOTH OPTICAL SURFACES

ALL DIMENSIONS ARE IN THE FORM $\frac{[in]}{mm}$.

THIS DRAWING IS FOR INFORMATION ONLY
NOT INTENDED FOR MANUFACTURING

	NAME	DATE
DRAWN	WD	9/16/2009
ENG APPR.	MG	9/22/2009
MFG APPR.	DD	9/30/2009

THORLABS INC. PO BOX 366 NEWTON NJ

TITLE: D=50.8mm, F=75.0mm,
VISIBLE ACHROMAT, 400nm-700nm

MATERIAL: E-BAF11 & N-SF11

SIZE A | REV. A

SCALE: 1:1 | SHEET 1 OF 1

DWG. NO. 20539-E01 | PART NO. AC508-075-A

THIS PAGE INTENTIONALLY LEFT BLANK

APPENDIX E. BICONVEX LENS SPECIFICATIONS

Details & Specs | Drawings | Literature & Downloads | Related Products

The KBX046AR.14 N-BK7 Bi-Convex Lens is a 1 inch (25.4 mm) diameter, 430 to 700 nm anti-reflection coated, N-BK7 bi-convex lens with an effective focal length of 25.4 mm. It is designed to meet the demanding requirements of laser electro-optic applications. Newport's N-BK7 precision bi-convex lenses are manufactured from fine annealed optical glass and are polished to tight tolerances using master test plates to ensure minimum wavefront distortion.

Model	**KBX046AR.14**
Lens Shape	Bi-Convex
Diameter	1.00 in. (25.4 mm)
Lens Material	N-BK7
Antireflection Coating	430-700 nm
Effective Focal Length	25.4 mm
Surface Quality	40-20 scratch-dig
Surface Accuracy, Power (lambda)	1.5 λ
Surface Accuracy, Irregularity (lambda)	λ/4
f/#	1.0
R	24.397 mm
Centration, Spherical Lenses	≤3 arc min
Center Thickness	10.132 mm
T_e	3.0 mm
BFL	21.80 mm
P_2	-3.59 mm
P_1	3.59 mm
Clear Aperture	≥central 90% of diameter
Chamfers	0–0.8 mm face width
Chamfers Angle/Tolerance	45° ±15°, typical
Center Thickness (T_c) Tolerance	±0.1 mm
Diameter Tolerance	+0/-0.1 mm
Focal length tolerance	±1 %
Coating Type	Visible Multilayer
Coating Code	AR.14

Newport
Experience | Solutions

View All Newport

Related Products: View All

Plano-Convex N-BK7 Cylindrical Lens, 50.8x25.4mm, 38.1mm FL, 430-700nm
Model: **CKX038AR.14**

Universal Fixed Lens Mount, 5.0 to 46.2 mm Diameter
Model: **AC-1A**

Gloves, Large, 100 Quantity
Model: **LAB-06**

Broadband Non-Polarizing Beamsplitter Cube, 25.4 mm, 400-700 nm
Model: **10BC17MB.1**

View All Related Products

THIS PAGE INTENTIONALLY LEFT BLANK

LIST OF REFERENCES

[1] J. F. Federici, B. Schulkin, F. Huang, D. Gary, R. Barat, F. Oliveira, and D. Zimdars, “THz imaging and sensing for security applications–explosives, weapons, and drugs,” in *Semiconductor Science Technology*, vol. 20, pp. S266–S280, Jun. 2005.

[2] S. M. Kim, F. Hatami, J. S. Harris, A. W. Kurian, J. Ford, D. King, G. Scalari, M. Giovannini, N. Hoyler, J. Faist, and G. Harris, “Biomedical terahertz imaging with a quantum cascade laser,” *Appl. Phys. Lett*., vol. 88, pp. 153903, Apr. 2006.

[3] Duke University, “Willie Padilla: Exploring technology’s ‘terahertz gap,’” [Online]. Available: http://pratt.duke.edu/news/willie-padilla-exploring-technologys-terahertz-gap [Accessed: 5 April 2016].

[4] Michael J. Fitch and Robert Osiander, “Terahertz waves for communications and sensing,” *Johns Hopkins APL Technical Digest*, vol. 25, no. 4, pp. 348–354, Oct.–Dec. 2004.

[5] J. E. Bjarnason, T. L. J. Chan, A. W. M. Lee, M. A. Celis, and E. R. Brown, “Millimeter-wave, terahertz, and mid-infrared transmission through common clothing,” in *Appl. Phys. Lett*., vol. 85, pp. 519, Jul. 2004.

[6] D. Zimdars and J. White, “Terahertz reflection imaging for package and personnel inspection,” in *Proceedings SPIE*, 2005, vol. 5781, pp. 78–83.

[7] J. Federici, D. Gary, R. Barat, D. Zimdars and J. White, “THz standoff detection and imaging of explosives and weapons,” in *Proceedings SPIE*, 2004, vol. 5411, pp. 75–84.

[8] L. Ho, M. Pepper, and P. Taday, “Terahertz spectroscopy: signatures and fingerprints,” *Nature Photonics*, vol. 2, pp. 541–543, Sep. 2008.

[9] Y. Sin, M. Sy, Y. Wang, A. Ahuja, Y. Zhang, and E. Pickwell-MacPherson, “A promising diagnostic method: terahertz pulsed imaging and spectroscopy,” *World Journal of Radiology*, vol. 3, no. 3, pp. 55–65, Mar. 2011.

[10] Teraview, “Terahertz for oral healthcare applications,” [Online]. Available: http://www.teraview.com/applications/medical/oral-healthcare.html. [Accessed: 8 April 2016].

[11] J. Federici and L. Moeller, “Review of terahertz and subterahertz wireless communications,” *Journal of Appl. Phys*., vol. 107, pp. 111101, Jun. 2010.

[12] S. A. Carn, *Scattering lecture slides*, Michigan Technological University [Online]. Available: http://www.geo.mtu.edu/~scarn/teaching/GE4250/scattering_lecture_slides.pdf [Accessed: 5 April 2016].

[13] D. Nüßler, H. Essen, N. von Wahl, R. Zimmermann, S. Rötzel, and I. Willms, “Millimeter wave propagation through dust,” in *Proceedings SPIE, 2008*, vol. 7108, pp. 710806-710806-6.

[14] F. Alves, B. Kearney, D. Grbovic, N.V. Lavrik, and G. Karunasiri, “Strong terahertz absorption using SiO2/Al based metamaterial structures,” *App. Phys. Lett*., vol. 100, pp. 111104, Mar. 2012.

[15] E. Montagner, “Optical readout system for bi-material terahertz sensors,” M.S thesis, Naval Postgraduate School, Monterey, CA, 2011.

[16] F. Alves, B. Kearney, D. Grbovic, N.V. Lavrik, and G. Karunasiri, “Bi-material terahertz sensors using metamaterial structures,” *Optical Society of America*, vol. 21, no. 11, Jun. 2013.

INITIAL DISTRIBUTION LIST

1. Defense Technical Information Center
   Ft. Belvoir, Virginia

2. Dudley Knox Library
   Naval Postgraduate School
   Monterey, California